A Statistical Analysis of Ionospheric Echoes Detected by the TIGER SuperDARN Radar

Brendan Doherty

Supervisors

Dr M.L. Parkinson

Professor P.L. Dyson

In partial fulfilment of the requirements for the degree

Bachelor of Space Science with Honours

In the subject of

Physics

School of Physics

La Trobe University

Bundoora, Victoria

November 2004

Abstract

SuperDARN HF backscatter radars measure the power (signal-to-noise ratio) and line-of-sight Doppler velocity and spectral width of echoes backscattered from 10-m scale irregularities in the high-latitude ionosphere. Occurrence statistics of these echoes were compiled for the TIGER Tasmanian SuperDARN radar (147.2°E, 43.4°S geographic; $-54.6°\Lambda$) for the four-year interval of declining solar activity, 2000 to 2003. The occurrence rates tended to decline with solar activity throughout the study interval. This was at least partly due to lower F-region plasma densities and thus weaker refraction restricting access to field-aligned irregularities. When sorted according to season, the results tended to reveal enhanced occurrence rates during the equinoxes; this may be partly due to the familiar enhancement of F-region plasma density well known to occur at high and mid-latitudes. However, it is also well known that more geomagnetic storms occur near the equinoxes, probably because coupling between the solar wind and magnetosphere is more effective for near zero dipole tilt angles. Lastly, the nightside bands of peak occurrence rates associated with the polar cap and auroral oval tended to be shifted post-midnight, consistent with the role of the ionospheric slip velocity in the growth of gradient drift waves, as discussed by Tsunoda (1988) and Parkinson et al. (2003). A study of all the data recorded by all the Southern Hemisphere SuperDARN radars for the year 2000 confirmed the results obtained with TIGER, in addition to revealing interesting features related to their different locations. In closing, many factors were multiplied together to influence the variability in occurrence rates. This thesis represents a significant advance in identifying new relationships in the occurrence statistics and separating out the confounding factors, over an above the initial study by Parkinson et al. (2003).

Statement of Authorship

Except where reference is made in the text of the thesis, this thesis contains no material published elsewhere or extracted in whole or in part from a thesis submitted for the award of any another degree or diploma.

No other person's work has been used without due acknowledgement in the main text of the thesis.

The thesis has not been submitted for the award of any degree or diploma in any other tertiary institution.

Brendan Doherty

Acknowledgements

First, I would like to thank Dr Murray L. Parkinson and Prof. Peter L. Dyson, for giving me this opportunity. Your support and guidance allowed me to accomplish this successful thesis.

I would like to thank the academic staff at La Trobe University for there help in furthering my knowledge on subjects related to this thesis.

Robert, Kevin, Shane, Dave, Barry and Alina, my fellow honours students; you have provided a valuable sounding board, this year could not have been attempted without them.

Naomi, *thank you* for putting up with me, you've kept me sane throughout a challenging time.

My family and friends, whom without I wouldn't have had the support to be where I am today.

Lastly and by no means least the inventor of sweet, marvelous and amazing chocolate. I owe you more then words can say.

CONTENTS

Chapter 1: INTRODUCTION

1.1 Geospace

The Sun plays an important role in a number of complex processes occurring in the ionosphere and upper atmosphere. The region considered as 'space' between the Earth and the Sun is actually extremely dynamic, filled with highly energetic particles and fields. The Sun continually emits its atmosphere in the form of fluctuating clouds of fully ionised gas or plasma, called the 'solar wind'. The solar wind is a hot, magnetised, supersonic, and highly conducting medium which also carries a weak magnetic field amounting to a few nanoTeslas (nT); this is called the Interplanetary Magnetic Field (IMF). Put simply, the field is said to be 'frozen in' to the plasma because the electrical conductivity of the plasma is very large, so that relative motion between the plasma and magnetic field becomes virtually impossible (Hargreaves 1992).
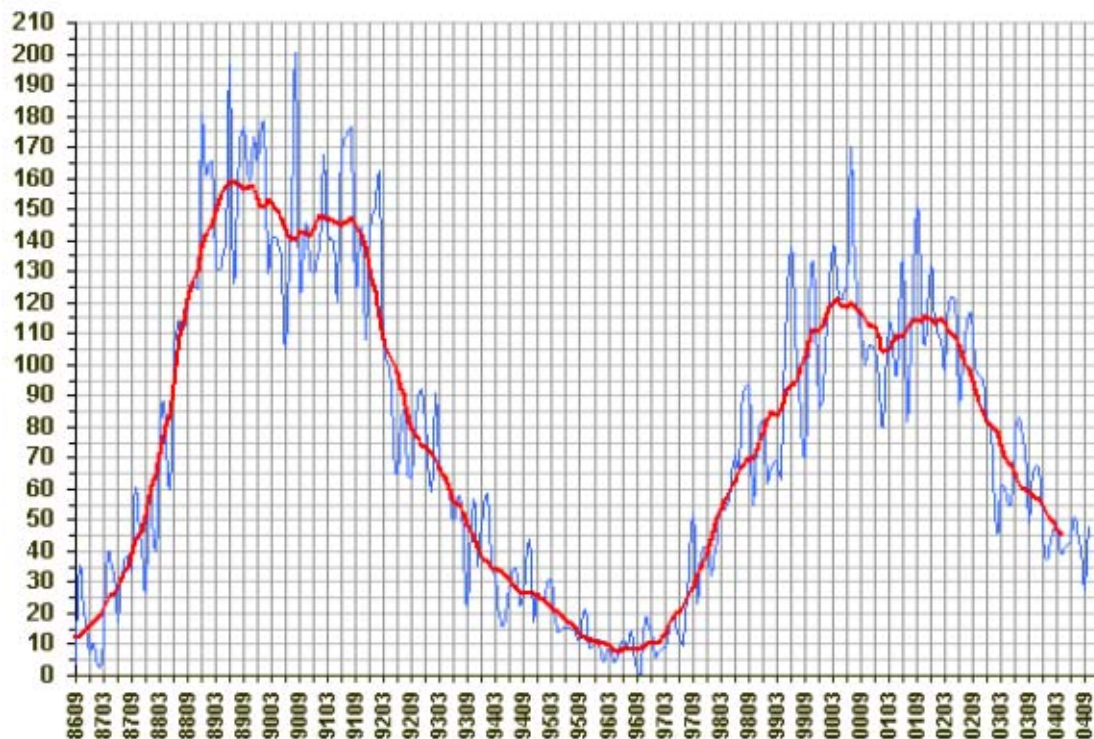
Figure 1.1: Solar Cycles 22-23. The red line is the monthly smoothed sunspot number while the blue line is the actual monthly sunspot number. Cycle 23 started in May 1996 with the monthly SSN at 8.0 and peaked in April 2000 at 120.8. The last smoothed monthly sunspot number is for April 2004 at 45.5. (Courtesy of Alvestad, 2004)

Figure 1.1 shows average monthly sunspot numbers and smoothed monthly average sunspot numbers from September 1986 to October 2004. The second major peak on the graph corresponds to the beginning of the period of study. A small decline before a secondary lower maximum and then a longer term decline should have an effect on the ionosphere and the data recorded by any SuperDARN radar.

The region of space immediately surrounding the Earth consisting of the foreshock, bowshock, magnetosphere, and ionosphere is called "geospace". Geospace is a very dynamic region undergoing almost continual change as the solar wind responds to highly variable processes occurring within the various layers of the Sun. The solar wind and its imbedded IMF reaches the Earth's magnetic field and sets off a variety of complex interactions, many of which are not yet fully understood. The processes include the reconnection between the IMF and the Earth's magnetic field, redirection of plasma along the magnetopause to the polar cusps, and magnetic storms that modify ionospheric convection and intensify the aurora.

The solar wind impinges on the Earth's magnetic field, compressing it on the dayside and extending the nightside magnetotail well into space, as seen in Figure 1.2. Coupling between the plasma of the solar wind and the magnetosphere generates a potential difference across the geomagnetic field. Because of the large parallel conductivity of the geomagnetic field lines, magnetospheric electric fields map down to the ionosphere, where plasma convection, frictional heating, and plasma instabilities occur.

The prevailing dawn-to-dusk electric field drives an antisunward $\mathbf{E} \times \mathbf{B}$ convection across the polar ionosphere. The electrical circuit is closed by large-scale and filamentary field-aligned currents (FAC). The resulting ionospheric electric field drives the F-region plasma at the Hall drift velocity given by,

$$v = \frac{E \times B}{B^2} \tag{1.1}$$

This produces the typical plasma convection patterns that are observed with SuperDARN radars.
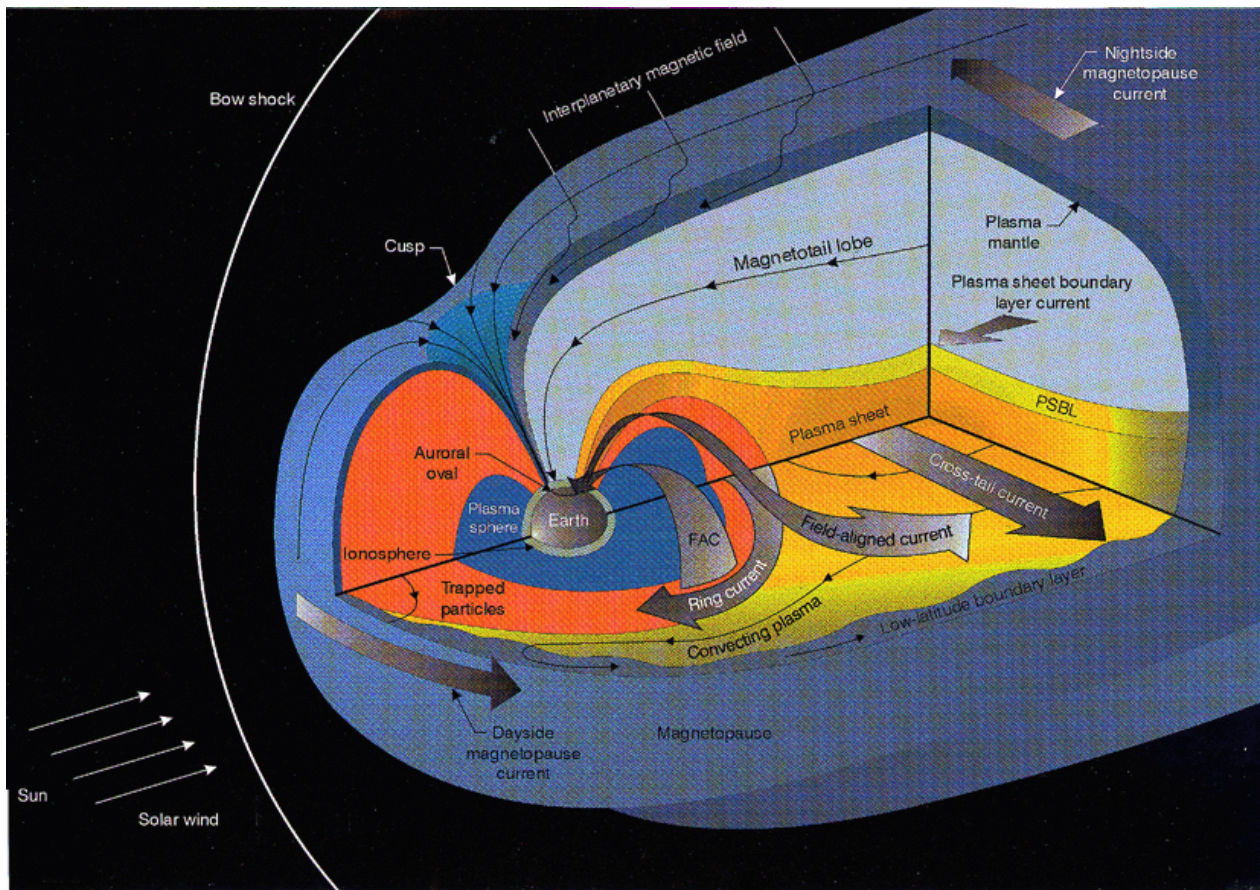
Figure 1.2: Schematic of the magnetosphere (from Høymork, 2000).

Ionospheric convection, aurora, and magnetic storms are some of the many phenomenon occuring at high latitudes that derive their energy from solar wind-magnetosphere interactions. Distinct signatures at various scales occur in the ionosphere, and they are highly variable in both time and space. In general, the plasma and IMF conditions in the solar wind, as well as changes in the geomagnetic field, should always be considered when analysing ionospheric processes.

1.2 The Earth's ionosphere

The ionosphere is a complex region of the Earth's atmosphere classified by its composition and vertical structure. Solar UV and X-Ray radiation creates a partially ionized plasma (less than 0.1%) which is electrically neutral to a very good approximation. The ionosphere contains localised enhancements and depletions of plasma arising from the competition between production, loss, diffusion, and transport of charge. The ionised plasma greatly influences the dynamics of the neutral atmosphere through collisional and heating processes.

Table 1.1: Characteristics of the daytime ionospheric layers (Hargreaves, 1992).

Region	Height (km)	Electron Density (m^{-3})
D	60-90	10^8-10^{10}
E	90-150	10^{11}
F1	150-210	10^{11}-10^{12}
F2	210-1500	Several 10^{12}

The vertical structure of the ionosphere is described in terms of four main regions defined by their photochemistry. The resulting heights and electron density are given in Table 1.1, and the various layers are depicted in Figure 1.3, which highlights each region by their respective peak electron density. The peak densities arise from the balance between production, recombination, and diffusion of the charged particles. The density of the neutral atmosphere decreases with height. Therefore, less gas is available for ionisation at greater altitudes, and very low plasma densities occur in the topside F2 region.

In general, the electron density profiles are very dynamic. For example, clear solar cycle effects can be seen. The average densities are higher during solar maximum years than during the solar minimum years. There is also a diurnal variability controlled by the solar-zenith angle. At night D, E, and F1 layers usually disappear, with the F1 layer merging into the F2 layer, despite a reduction in its density. Auroral

E and sporadic E layers occur during the night and help maintain this region. The D region is strongest during the day and is formed by X-Rays and cosmic rays.
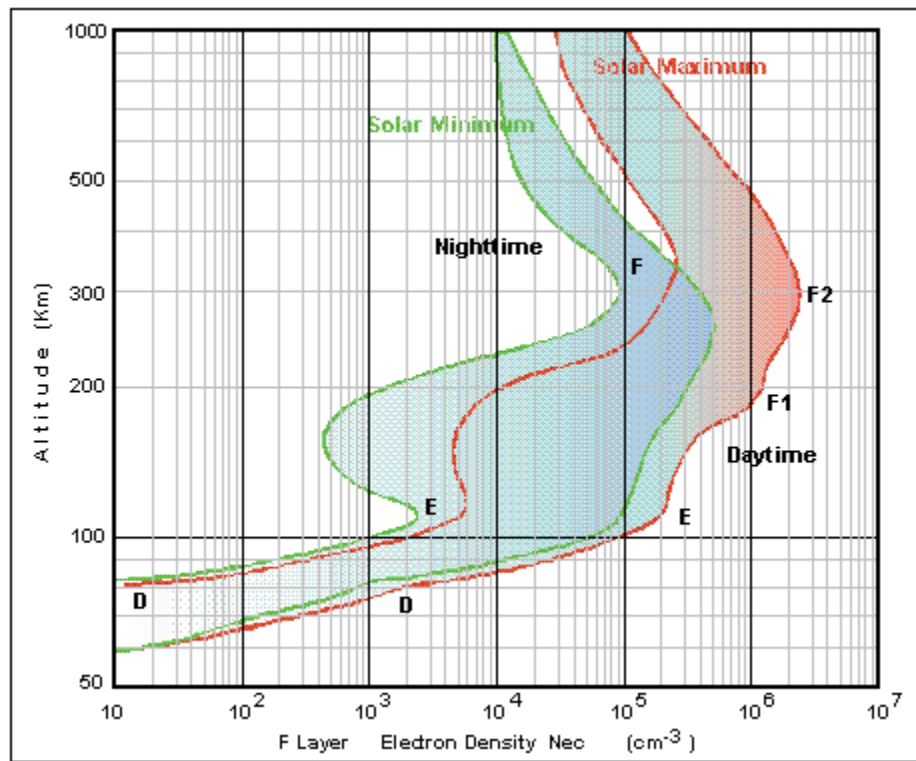
Figure 1.3: Vertical profile of the ionosphere showing electron densities and highlighting the difference between solar maximum and minimum, and night and day conditions (Balthazar, 2004).

1.3 Ionospheric instabilities and irregularities

The E layer plasma is partly magnetised and the F layer plasma is strongly magnetised. These different plasmas are capable of supporting a variety of wave motions which characterise instabilities in the plasma density. These often originate as small initial perturbations in the plasma which subsequently grow to large amplitudes. Important considerations when dealing with instabilities include the physical mechanism, their growth and decay rates, and the thresholds for the instabilities to occur. Many mechanisms have been proposed to account for the growth and decay of plasma density structures in the high-latitude ionosphere (Kelly et al., 1982).

Two primary plasma instabilities are thought to create irregularities at high latitudes (Tsunoda, 1988). These are the two-stream Farley-Buneman instability (which

5

produces Type I Doppler spectra) and the **E×B** gradient drift or fluid interchange instability (which produces Type II Doppler spectra). The two-stream instability occurs when electrons and ions counter stream with a velocity greater than the ion-acoustic speed, C_s ,defined by,

$$C_s = \left(\frac{k_b \left(T_i + T_e \right)}{m_i} \right)^{\frac{1}{2}}$$

(1.2)

Where T_i and T_e are the ion and electron temperatures, k_b is Boltzmans constant and m_i is the ion mass (Chen, 1984). The waves produced by this instability propagate nearly perpendicular to the magnetic field. This instability grows more rapidly at shorter wavelengths. The importance of this instability is greatest in the E-region at low and high latitudes (Hargreaves, 1992).

The gradient drift instability, similar to the Rayleigh-Taylor instability, occurs when an external force (e.g. electric field, neutral winds, or gravity) acts to produce a small perturbation on a region of enhancement plasma density. A charge separation takes place in the presence of the magnetic field, leading to an initially small "polarization electric field" which, due to the presence of a magnetic field, acts to enhance the initial perturbation. The feedback process leads to the rapid growth of irregularities. This instability is a common mechanism by which irregular structures in the F-region break down into smaller ones (Hargreaves, 1992).

It is believed that intense small-scale irregularities are created by convection phenomena and interchange instabilities that operate on steep transverse gradients, that characterise the walls of large-scale plasma structures (Tsunoda, 1988). SuperDARN radars are capable of detecting decametre-scale irregularities when they are created in the presence of sharp plasma density gradients occurring in the auroral and polar cap ionosphere. It is also believed that decametre-scale iregularities dissipate in seconds through cross field diffusion enhanced by ionospheric Pedersen conductance. Therefore, they can only exist in regions where strong irregularity growth counteracts rapid decay, and they cannot convect to great distances beyond their generation point.

1.4 The Super Dual Auroral Radar Network (SuperDARN)

The Super Dual Auroral Radar Network (SuperDARN) consists of a group of oblique sounding, mono-static coherent radars sensitive to Bragg backscatter from decametre-scale electron density irregularities in the ionosphere (Greenwald, 1995). SuperDARN presently consists of 16 radars located in the Northern and Southern Hemispheres at high latitudes encircling the magnetic poles. These radars were created to observe the auroral and polar cap ionospheres, providing a global view of the configuration and dynamics of plasma convection in the high-latitude ionosphere

SuperDARN radars rely on the backscatter of obliquely propagating radio waves off ionospheric irregularities which are aligned parallel to the Earth's magnetic field. A single SuperDARN antenna array consists of 16 elements which facilitate scans through 16 beam directions separated by 3.24° to form a 52° azimuthal field of view.
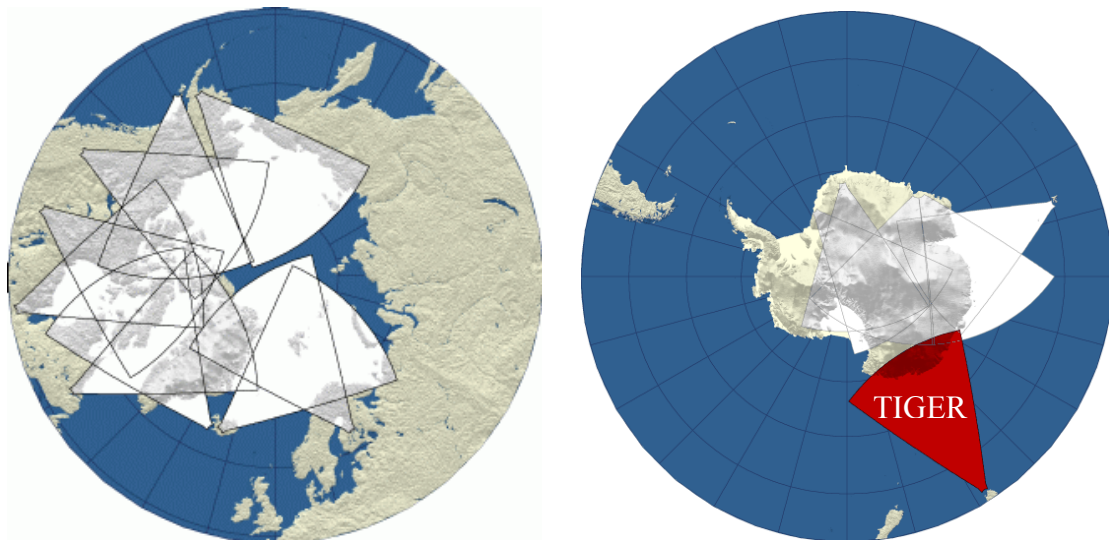
Figure 1.4: Location of all the SuperDARN radars and their fields of view (R. Barnes, Applied Physics Laboratory).

The radars rely on ionospheric refraction to achieve orthogonality with the magnetic field. To adjust for the effects of changing electron density on refraction, the radars are capable of dynamic frequency selection over the range 8 to 20 MHz (wavelengths 38 to 17 m). The radars can detect Bragg backscatter from ionospheric irregularities having a wavelength equal to one half of the radar wavelength, which corresponds to an irregularity scale size of 18 to 13.5 m. A full description of SuperDARN radars can be found in papers such as those written by Greenwald et al., (1985, 1995).

1.5 The Tasman International Geospace Environmental Radar (TIGER)

The Tasman International Geospace Environment Radar (TIGER) concept involves two component radars that can operate individually, as a coordinated pair, and as part of SuperDARN (Dyson and Devlin, 2000). The TIGER radars are located at lower geomagnetic latitudes than the other SuperDARN radars, and cover an area of sub-auroral to polar cap latitudes located south of Australia and New Zealand. The first of the pair, TIGER Tasmania, has been operating since 1999, and is located on Bruny Island (147.2°E, 43.4°S), off the south coast of Tasmania. Its counterpart located near Invercargill, New Zealand, has just been installed. Whenever TIGER is mentioned it shall mean the TIGER radar in Tasmania where its location and field of view can be noted in Figure 1.4 (shown in red).

Figure 1.5: The 16 element transmitting and receiving array (left), and the four element interferometer receiving array (right).

TIGER (Fig. 1.5) is based on an existing SuperDARN radar design and is capable of studying ionospheric scatter and sea scatter. TIGER relies on the backscatter of HF radio waves from ionospheric irregularities and the sea surface, and it routinely determines the Doppler characteristics of the returned signals. The radio waves are transmitted across a spread of elevation angles, so that they undergo ionospheric refraction and arrive orthogonally to magnetic field-aligned irregularities located across a broad range of group delay.

TIGER's transmitting and receiving array consists of 16 log periodic, horizontally polarised antennas, forming a narrow azimuthal beam that is scanned across the radar

footprint in 16 steps covering 52°. The maximum range is 3330 km. The radar is operated at a frequency between 8 and 20 MHz. Most ionospheric echoes are observed at frequencies of 12 MHz, sometimes less at night, and at somewhat higher frequencies during the day (Dyson and Devlin, 2000). This is because the electron density increases considerably during the day due to photo-ionization of the atmosphere by sunlight. An additional four antennas form an interferometer to measure the elevation angle of backscattered signals. Although SuperDARN radars are operated 24 hours a day, 365 days a year, the amount of scatter observed by any radar is highly variable.

TIGER transmits a sequence of pulses at different spacings, as shown in Fig. 1.6 in which the pulse spacing is varied from pulse to pulse. The pulse set length has a duration of ~88 ms and integration times of 3 s and 7 s are commonly used. By using the lags between $1t_o$ and $18t_o$ an autocorrelation function (ACF) can be constructed for the returned signal. ACF's of the echoes at each range are calculated and averaged over an integration time of 7 seconds. These ACF's can be analysed in near real time using the 'FITACF' algorithm, and the results are stored in .*fit* files. Data from the .*fit* files were used to create the databases used in this study. These databases will be analysed to reveal changes in key echo parameters including occurrence rates (%), backscatter power (signal-to-noise ratio) (dB), line-of-sight Doppler velocity (ms^{-1}), spectral width (ms^{-1}), and elevation angle (°) (Greenwald, 1985; Dyson and Devlin, 2000; Dyson et al, 2003).
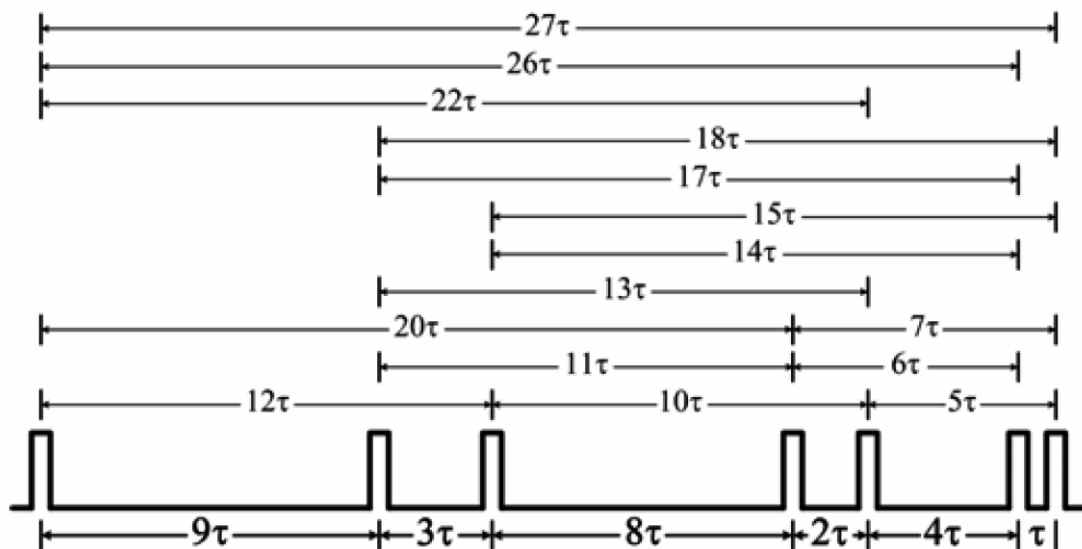
Figure 1.6: An example of the standard pulse set used by TIGER (Dyson et al., 2003).

Backscatter power is a measure of the signal-to-noise ratio and in this study had to be >3 dB for the signal to qualify as an echo. In the simplest interpretation, line-of-sight Doppler velocity is a direct measure of the **E×B** drift of irregularities when they backscatter the HF signal. Similarly, in the simplest interpretation, spectral width is an estimate of the spread in the Doppler velocity which arises because there are many irregularities in a given range cell drifting at different **E×B** speeds. Elevation angles are measured with the 4 element interferometer array, but were not analysed in this report. Figure 1.7 is a typical summary plot, taken from the TIGER summary data web page at the University of Newcastle.
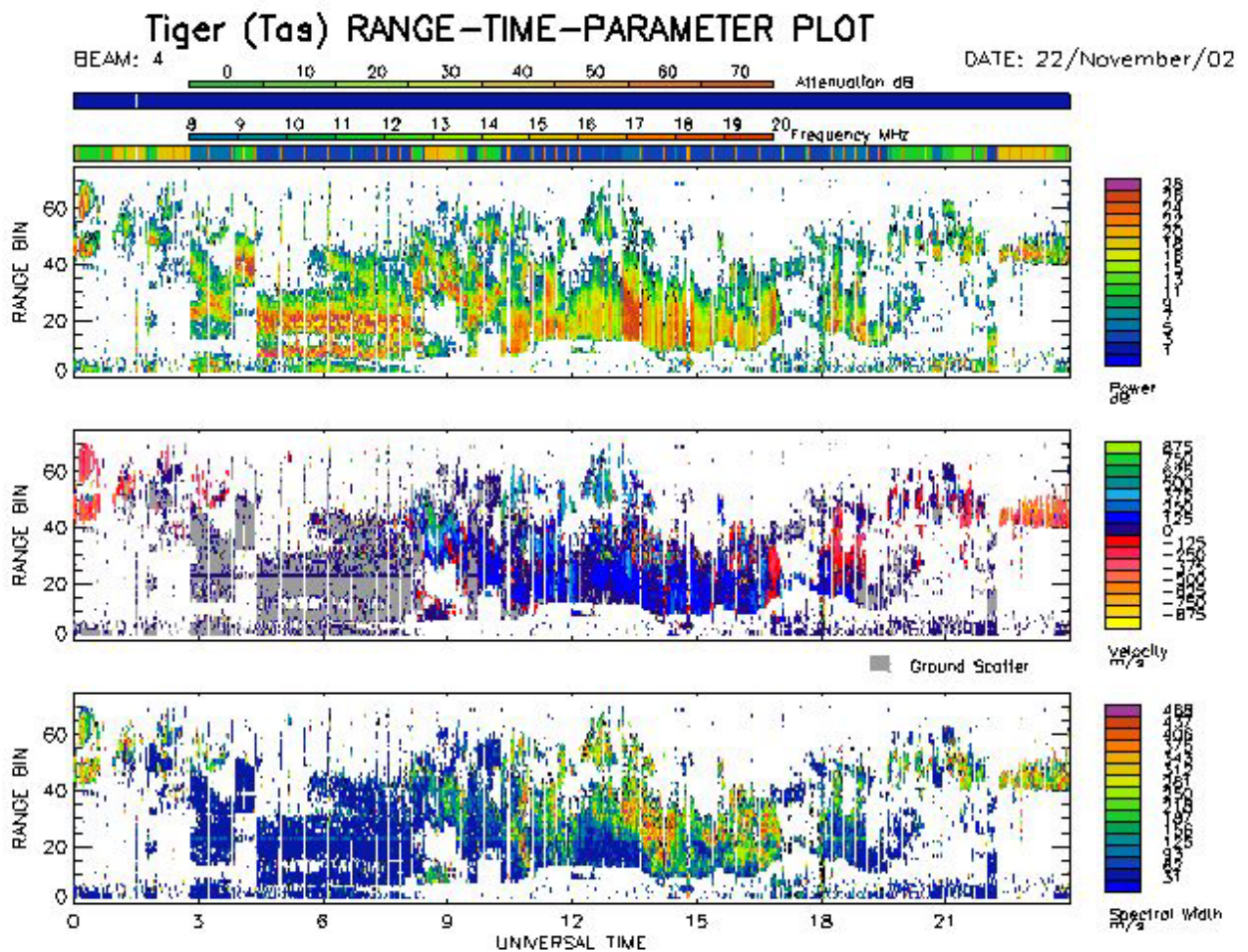
Figure 1.7: TIGER summary plot showing the (a) backscatter power (dB), (b) line-of-sight Doppler velocity (ms^{-1}), and (c) spectral width (ms^{-1}) for the 22nd November 2002 (courtesy of http://plasma.newcastle.edu.au/spwg/research/tiger/sdata.htm)

1.6 HF radio wave propagation

The E- and F-region ionosphere supports the propagation of HF radio waves, whereas ionospheric absorption tends to be strongest in the D region. Ionospheric characteristics vary with solar cycle, season, and the time of day. Hence HF propagation conditions are highly variable, and the frequency must be constantly adjusted to fulfill a given task. For this reason, SuperDARN radars are frequency agile over the HF band. The HF radio wavelengths are short enough that the ionospheric medium does not change much in the distance of a few wavelengths, and can therefore be approximated by a plane stratified medium, as indicated in Figure 1.8. Since the plasma frequency increases with height, the refractive index n becomes smaller, and the ray gradually bends toward the horizontal.
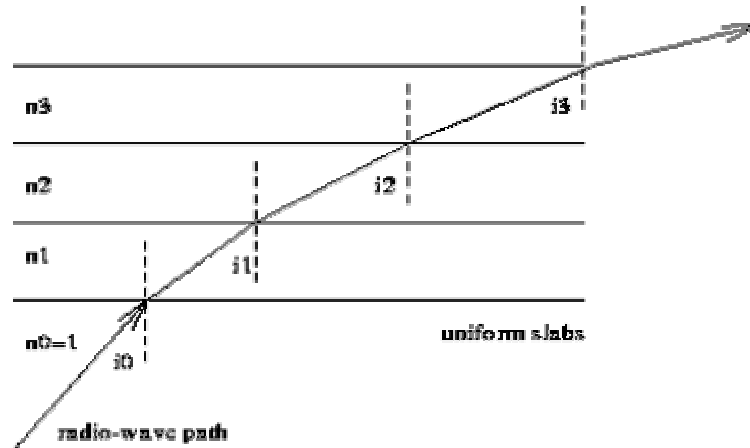
Figure 1.8: Refraction of a HF ray path in a plane stratified ionosphere.

Figure 1.9 demonstrates that for a single transmission frequency, the group range of the ray path varies with elevation angle, and often a single layer supports propagation to a single location via two different ray paths. The ionosphere is also birefringent, supporting both ordinary and extraordinary propagation modes. This also adds to the number of rays which can propagate to a single location.

Rays with an elevation angle above some critical value, break through the ionosphere and never return to the Earth. Rays with an elevation angle less than this critical value are reflected either at E- or F-layer apogee heights; these rays will then hit the ground and may be scattered back along the same path to the receiver. Echoes obtained via these ray paths are called *ground scatter*. Alternatively, these rays can be reflected from the Earth back up to the ionosphere, and then back to the Earth. Scatter from

ionospheric irregularities occurs whenever the rays are perpendicular to the field lines and the irregularities are sufficiently intense. Ionospheric scatter may emanate from "half hop", "one-and-a-half hop", "two-and-a-half hop" modes, etc.
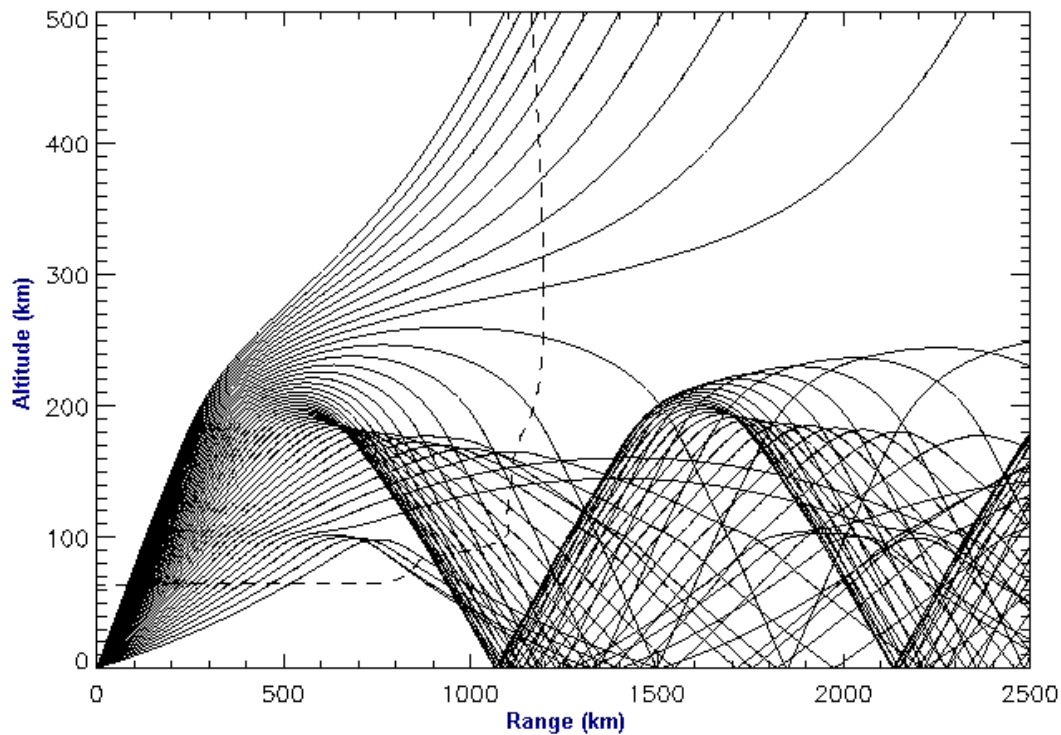
Figure 1.9: Computed ray paths through a model ionosphere for a HF frequency of 12.45 MHz and elevation angles from 5° to 50°.

The ability of SuperDARN radars to detect ionospheric irregularities is a product of a number of factors, many of which have been outlined previously, including solar activity, the solar wind, IMF conditions, coupling of the ionosphere to the magnetosphere, time of year and the time of day. Many factors also affect the propagation conditions of HF radio waves through the ionosphere. This thesis aims to clarify the cause and some of these effects, by using statistical relationships to determine some of the main characteristics of the high latitude ionosphere.

Chapter 2: **EXPERIMENT AND ANALYSIS**

SuperDARN radars provide a very useful way of studying large scale dynamic processes in the high-latitude magnetospheric-ionosphere system. TIGER began operation in December 1999, and since then has been observing the structure and dynamics of plasma convection and electric fields in the auroral and polar cap regions. TIGER is especially well suited to the study of auroral processes since the other SuperDARN radars are located further poleward and the auroral oval often expands equatorward of their fields of view during geomagnetic storms.

All of the available data from TIGER was studied for a four year period, from January 2000 to December 2003, which corresponds to an interval of declining solar activity. Solar maximum occurred during April 2000 and the next solar minimum is predicted to occur in 2006. There are various measures of solar activity, including but not limited to sunspot number and the 10.7-cm solar radio flux. Figure 2.1 shows the variability in sunspot number during the chosen study interval. Data on daily sunspot number was downloaded from the National Geophysical Data Center (NGDC) web site.

The Advanced Composition Explorer (ACE) spacecraft orbits the L1 libration point located ~230 Re upstream of the Earth in the solar wind (ACE 2003, Zielik 1995). ACE measures properties of the solar wind using a number of instruments. Two particular instruments and data products resulting from them were harnessed for the purpose of this study. The Solar Wind Electron, Proton, and Alpha Monitor (SWEPAM) measures the solar wind plasma electron and ion fluxes (rates of particle flow) as functions of direction and energy, and the ACE Magnetometer (ACEMAG) measures the local interplanetary magnetic field (IMF) direction and magnitude.
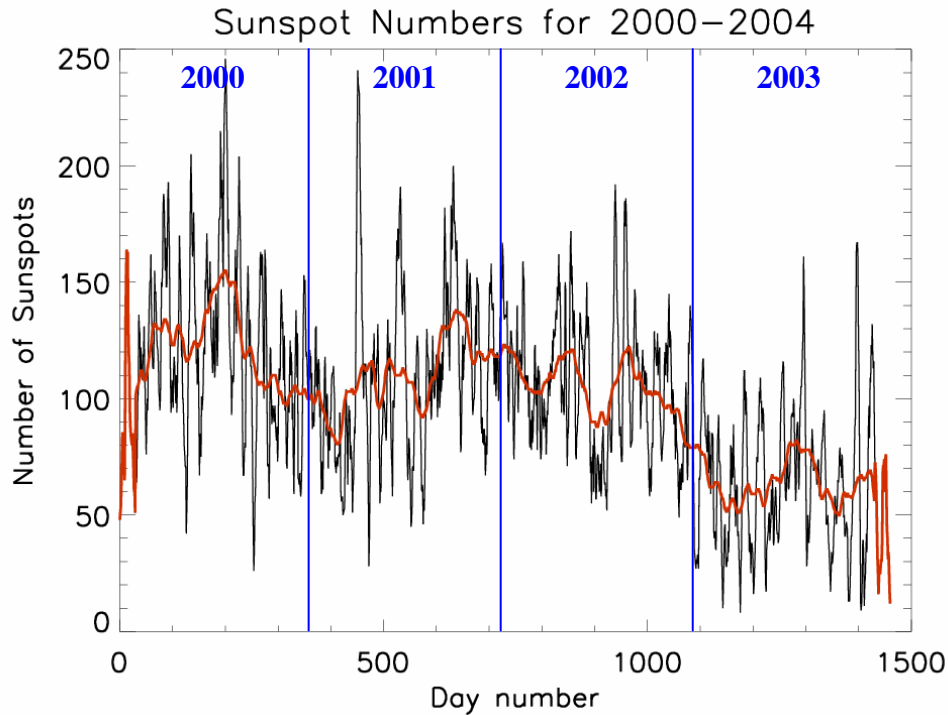
Figure 2.1: Daily (black) and 50-day running average (red) sunspot numbers. Blue vertical lines indicate the start of a new year.

The preceding parameters were incorporated in the database files generated in this study, and it is possible to sort the radar measurements according to them.

2.1 Radar operation

Like all SuperDARN radars, TIGER has two main types of operation, they fall under the headings of "common time" and "discretionary time." Common time means that each radar is looking at the ionosphere in the same way, whereas discretionary time allows the execution of experimental modes. In the common mode of operation, TIGER calculated the average ACF of echoes at 75 range gates starting at 180 km and separated by 45 km.

The FITACF algorithm processes the average ACF's to estimate key Doppler parameters for all ranges on every beam (section 1.5). TIGER's version of FITACF rejected echoes with signal-to-noise ratio less than 3 dB. The procedure basically tags echoes as "ground scatter" if the Doppler speeds and spectral widths are less than 30

ms^{-1} and 30 ms^{-1}, respectively. For the purpose of this study, ionospheric echoes were those defined by the FITACF algorithm.

TIGER began recording data in November of 1999 and since then has been operating nearly continuously. As with any experimental facility, there have been short term data losses due to computer crashes, power outages, and corrupted data files. Initially many of the transmitters failed due to faulty power supplies, but these were quickly redesigned and rarely fail. After the first year of operation, the radar was operated successfully for >90% of the time.

As previously explained, SuperDARN radars rely on the ionosphere refracting HF radio waves until they become orthogonal to magnetic field aligned irregularities, so the detection of echoes is related to the prevailing propagation conditions, as well as what is happening in the ionosphere. There is a preferred range window for the detection of backscatter determined by the prevailing propagation conditions. This is why it is so important to consider changes in the radar operating system and the scheduling of different radar control programs.

All SuperDARN radars run the same radar control program (RCP) during common time. TIGER's ran the RCPs called "normal_scan" and "fast_scan" before April 2002. The only difference between these two programs is in the integration time on each beam (7 s versus 3 s), and the resulting full-scan interval (1 min versus 2 min). A new radar operating system was installed in March 2002 and two new common time RCPs were installed in April 2002. These new common time RCPs were called "normal sound" and "fast sound." These new generations of RCPs were the same as the old ones, except for the addition of the "sounder mode" (University of Alaska Web Site). At the end of a 16-beam scan, the sounder mode scans through the available frequency bands to determine the frequency with the most ionospheric scatter for subsequent operation. These RCPs have greater frequency agility and a greater capacity to increase the amount of scatter during marginal propagation conditions.

2.2 Database

Data was obtained from two instruments onboard ACE. Firstly, the SWEPAM instrument provided hourly averaged solar wind parameters including the solar wind bulk velocity and density, and hence kinetic pressure. Secondly, the ACEMAG instrument provided the orientation and strength of the IMF averaged to 4-min resolution. Science level 2 data for these instruments was obtained from the ACE Science Center web site (ACE, 2003).

"K_pA_p" files were downloaded from the National Geophysical Data Center (NGDC) web site. They provided 3 hourly K_p indicies, sunspot number, and 10.7 cm solar radio flux. The K_p index is determined using a network of mid-latitude magnetometers, and is a logarithmic measure of planetary geomagnetic activity.

In this study, a year was considered to be a calendar year, from January to December. A season was considered as a regular season in a year, e.g. summer was a combination of data recorded during December, January, and February.

The data analysis procedures used to compile simplified databases and then sort and rapidly display the results are illustrated in Fig. 2.2. The RCPs and the FITACF program were written in the C programming language (Robin Barnes, Applied Physics Laboratory), and the subsequent database analysis was written using IDL (Interactive Data Language, Version 6.0). The main steps in the analysis are summarised as follow:

1. SuperDARN radars record data in many ways. At the most basic level, the raw ACFs of echoes received by the radar are recorded in *.dat* files. These data files are passed through the FITACF algorithm, generating files with the suffix *.fit*. Attached to each *.fit* file is an index file (*.inx*), which permits rapid parallel access to the *.fit* data. More than 200 gigabytes of *.fit*/*.inx* data from the four year intervals, January 2000 to December 2003, was obtained for TIGER.

2. A program called *"create_imf"* runs in IDL. It combines the data from the SWEPAM and ACEMAG instruments into a single binary *.imf* file.

3. A program called *"create_database,"* again written in IDL, was modified to take all the data collected on beam 4 of TIGER, and combine it with the KpAp and *.imf* files. In the process of combining the data, the program removed invalid FITACF results on the basis of whether the "quality flag" was set. The remaining useful data was saved to monthly files. After processing, the aforementioned 200 GB of data was reduced to about 45 GB.

4. To create data base files on other time scales, another program called *"merge_database"* was employed. This program was easily adapted to create seasonal and yearly files and 40 day files centered on the solstices and equinoxes. Yearly and seasonal files were created by merging monthly files.

5. Two more programs were employed and modified to create plots of various parameters. *"occurrence_rate"* plotted the occurrence of echoes, and *"average_fitacf"* was used to plot the average of FITACF parameters including the backscatter power (signal-to-noise ratio) (dB), line-of-sight Doppler velocity (ms^{-1}), spectral width (ms^{-1}), and elevation angle. These programs required the transformation between radar beam and range number to geomagnetic coordinates, and a conversion from universal time (UT) to magnetic local time (MLT). The transformation files were supplied by Dr. Colin Waters, the University of Newcastle.

Geomagnetic latitudes were defined using altitude adjusted corrected geomagnetic coordinates (AACGM) (Baker et al., 1989). The range gates were mapped to AACGM latitude using the standard method used by the SuperDARN community. This method assumes a virtual reflection height of 300 km, but with tapering to E-region heights at ranges <600 km. The difference between MLT and UT for beam 4 was taken to be 10 hrs and 46 min, but this difference changes rapidly approaching the geomagnetic pole, where the beam direction veers away from the magnetic meridian.
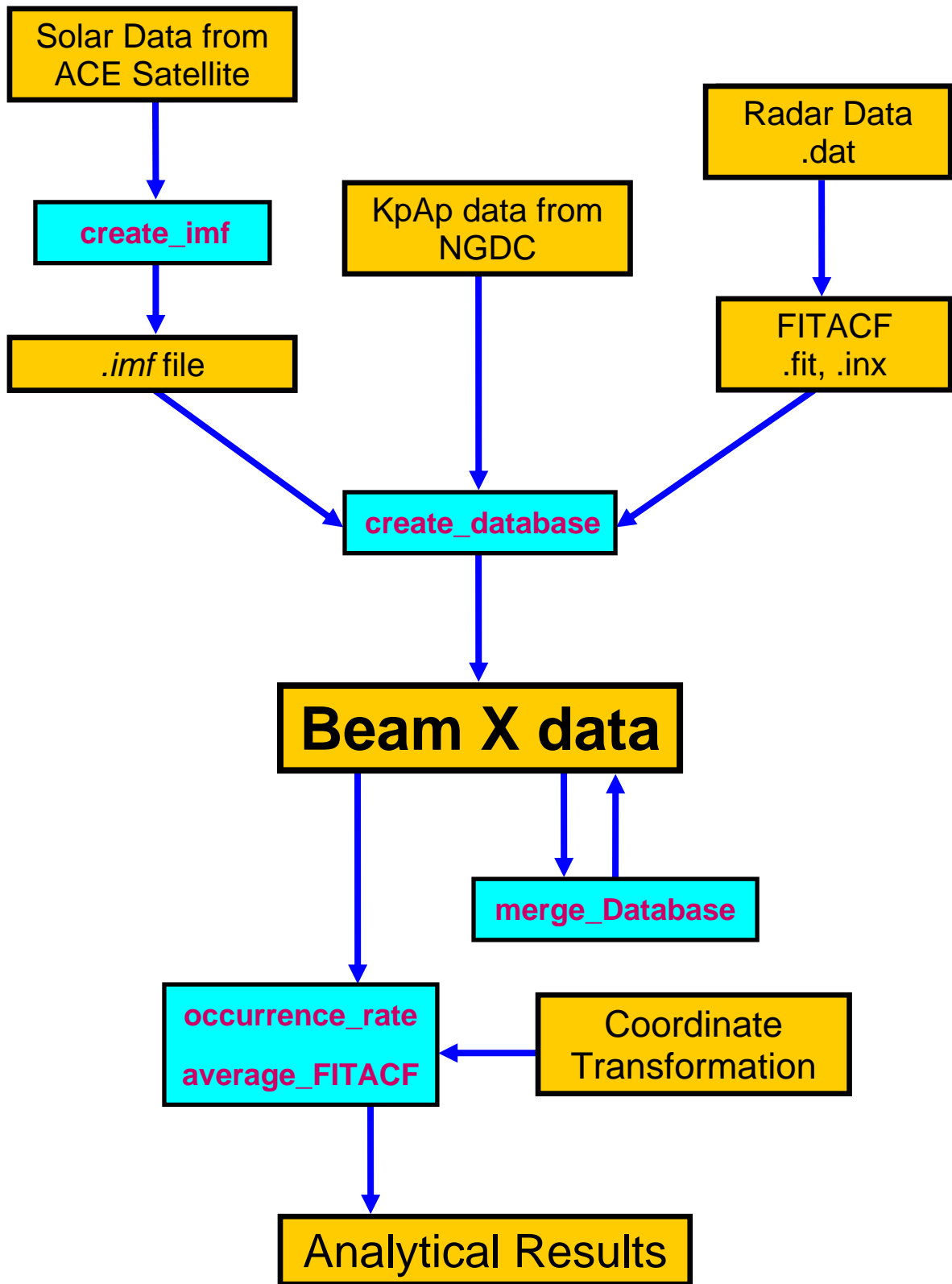
Figure 2.2: IDL and C language data analysis procedures.

All of the above programs could be easily modified to analyse data recorded on any beam of any SuperDARN radar. Figure 2.2 is a block diagram showing the processes outlined above.

2.3 Statistical moments

Statistics could have been compiled for all 16 beams combined, but this creates difficulties in separating geophysical and geometric dependencies. Moreover, the choice of a single beam for analysis resulted in an immediate 16-fold decrease in the amount of data to be analysed. Beam 4 was the chosen beam because it points along the magnetic meridian, covering the greatest number of geomagnetic latitudes, and providing an overview of dynamics occurring in the sub-auroral, auroral, and polar cap ionosphere. Beam 4 is a good choice because it reveals most of the interesting features observed throughout the entire radar field of view.

Occurrence rates were calculated by counting the total number of echoes during 15-min intervals of time at each of the 75 ranges, then dividing by the total number of soundings made on a particular beam. Data was binned in 15-min intervals of MLT, and in 75 range bins of width 45 km before mapping to magnetic latitude. Thus 96 time bins in a day $\times$ 75 ranges = 7200 bins in each occurrence plot.

In this study, only the first moments or the arithmetic means of the FITACF parameters were calculated. This was done in the following manner. If X_1, X_2, …, X_N are the N values of the samples X, the mean is defined as

$$\overline{X} = \frac{\sum X_N}{N}$$

(2.1)

The variable X corresponds to a FITACF parameter binned in the same way as the occurrence rates. Higher order statistical moments could be readily calculated in a future study. For example, maps of the modes, medians, and variances require calculation

The many factors which influence the rate of scattering occurrence and average FITACF parameters will be discussed in subsequent chapters.

Chapter 3: **RESULTS**

In this study, all of the available FITACF data for soundings made by TIGER between January 2000 and December 2003 was acquired. From this extensive data set, only key FITACF parameters for beam 4 were extracted to reduce the amount of data. Beam 4 was chosen because it is aligned along the magnetic meridian. As mentioned before, the data was passed through various programs, to eventually create statistical plots of the occurrence and Doppler characteristics of echoes. In the following sections, results are presented in the form of contour plots of echo occurrence and average FITACF parameter versus magnetic local time (MLT) and geomagnetic latitude (i.e., clock dial plots).

3.1 Occurrence rates of ionospheric echoes

Figure 3.1 shows occurrence rates averaged over each year. A comparison from one year to the next reveals similar patterns, but there is a general decrease in the maximum occurrence and the area of this maximum occurrence. This decrease is associated with a decline in solar activity over the four years. However, the decrease in the number of echoes was partly arrested during 2002 which had generally slighty higher scatter rates over a greater area. A striking feature is the drastic change in scatter occurrence from day (between 06 to 18 MLT) to night (between 18 to 06 MLT). The difference appears smaller in 2002 and 2003 due to the aforementioned change in radar operating programs.
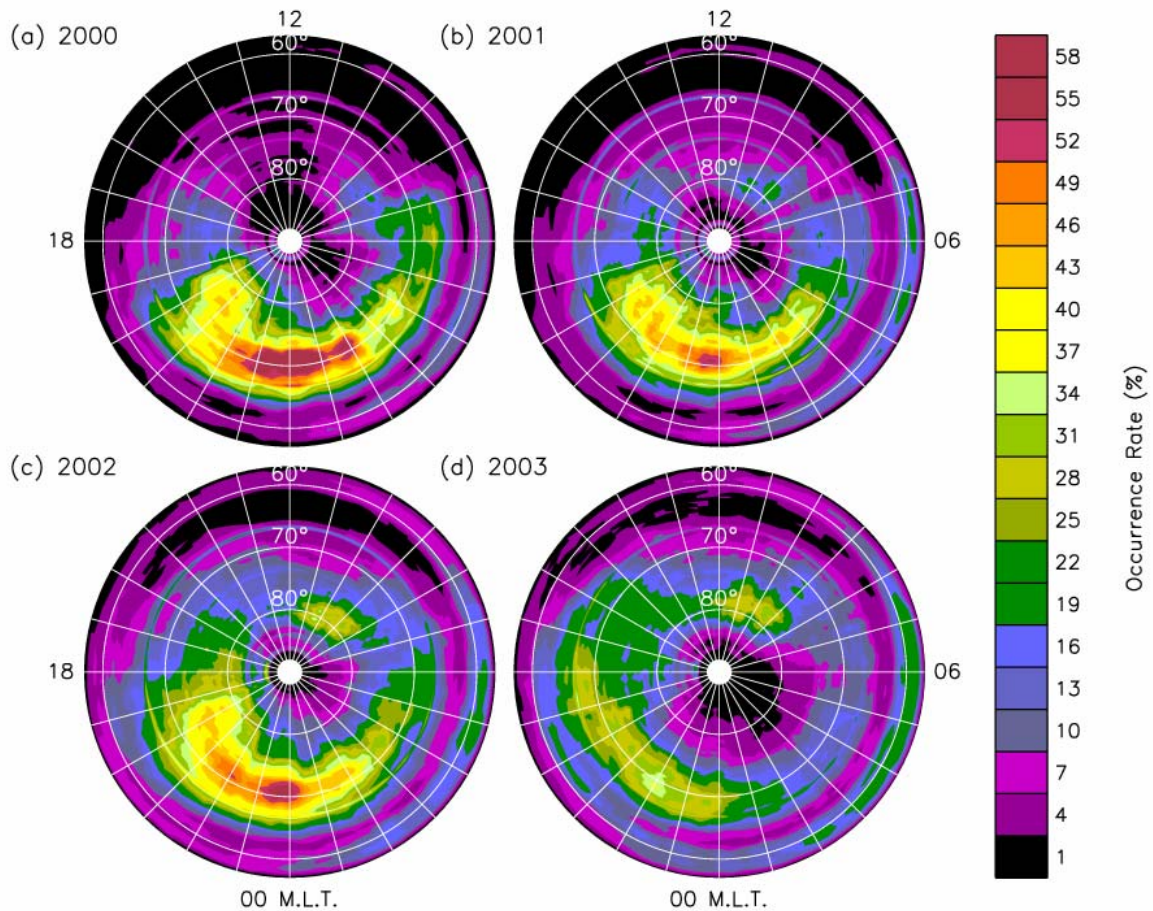
Figure 3.1: The occurrence rate of beam 4 ionospheric echoes for all *Kp* values detected during year (a) 2000, (b) 2001, (c) 2002, and (d) 2003. The results are shown versus MLT and magnetic latitude, with noon (12 MLT) at top, dusk (06 MLT) at right, and the equatorward boundary at −57° geomagnetic. Magnetic latitudes of −60°, −70° and −80° have been superimposed. No data were acquired poleward of −88°.

Through all years there is a local minimum in the occurrence rates represented by the rings of low occurrence rate centered on aproximately 62° latitude. Small bands of occurrence <20% were found in the pre-dawn to dawn sector equatorward of 60°. The occurrence rates were generally <7% at similar ranges for other MLTs. Scatter recorded at these ranges is generally considered to be due to E-region irregularities, and meteor trails.

Figure 3.2 (page 25) shows the relationship between ionospheric echoes and geomagnetic activity index K_p for all years of the study. Little statistical significance is yielded from studying K_p variations over the space of a single month. Larger Kp values are not as frequent as lower ones, and hence require more time to accumulate
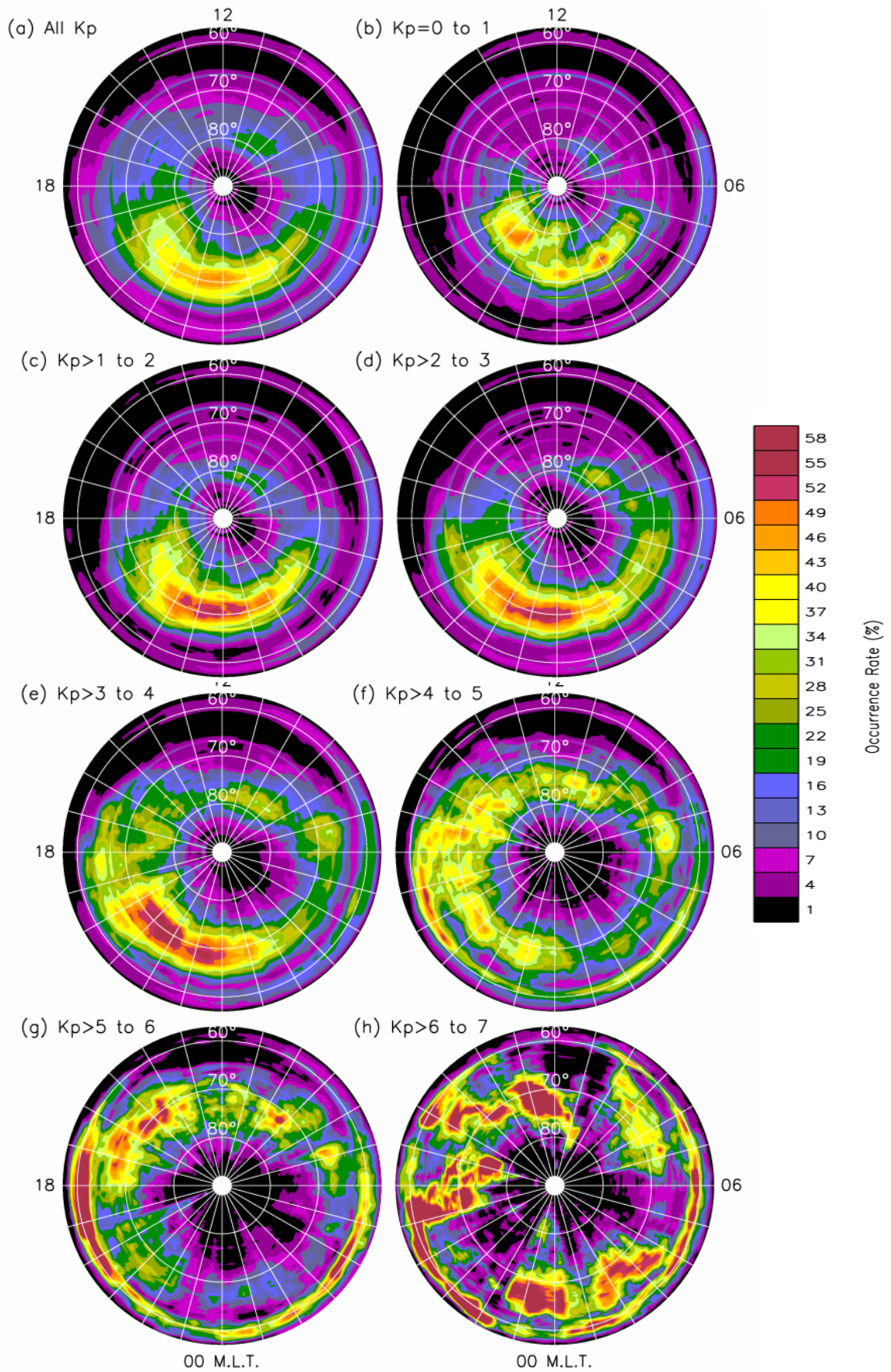
Figure 3.2: The occurrence rate of beam 4 ionospheric echoes detected during the entire study interval, and sorted according to geomagnetic activity (a) All K_p values, (b) $K_p = 0$ to 1, (c) $K_p > 1$ to 2, (d) $K_p > 2$ to 3, (e) $K_p > 3$ to 4, (f) $K_p > 4$ to 5, (g) $K_p > 5$ to 6 and (h) $K_p > 6$ to 7.

enough data to access the underlying average. Sorting the echo occurrence with respect to Kp using a single month of data yeilds insignificant results.

The occurrence rates averaged over all K_p values appear most in likeness to moderately disturbed conditions, $K_p = 2\sim3$ (c). As in Figure 3.1, peak occurrence rates were usually observed in the nightside auroral oval and polar cap ionosphere between $-65°$ and $-76°$. However, this was not the case for quiet and heavily disturbed conditions. During quiet conditions, $K_p = 0$ to 1, patches of polar cap echoes ($\sim72°$ to $82°$) were found between 20 and 02 MLT and contained similar rates of occurrence to the band found further equatorward from 21 to 03 MLT centred about $-71°$. For moderate K_p values (~2 to 3) the polar cap echoes were almost completely lost and replaced by the main band of auroral and polar cap echoes. Under increasingly disturbed conditions the main band of auroral and polar cap echoes became impossible to discern.

Overall the occurrence statistics show that for increasing geomagnetic activity the main patch of nightside echoes associated with the polar cap and particle precipitation in the auroral oval are displaced equatorward (however the auroral oval also expands poleward during substorms). The peak occurrence rates were constricted within a $\sim10°$ latitude band until very disturbed conditions ($K_p=5$ and greater), when they almost completely encircle the polar region. Many more echoes were observed in the afternoon to dusk sectors during very disturbed conditions. Similar variations in occurrence due to geophysical activity were obtained for all four years.

Figure 3.3 (page 27) shows plots of occurrence rates for the year 2000 sorted according to season. Similar patterns of occurrence were found for all seasons, but there were some features which distinguished one season from the next. Again one of the prevalent features was the relative difference between the dayside and nightside occurrence rates. It is clear that the majority of ionospheric echoes were recorded on the nightside, with generally less than 10% occurrence during the day.

In regards to the main feature on the nightside, the occurrence was roughly symmetric about the noon-midnight meridian. A clear maximum was concentrated near 00 MLT

and 70°, centred on midnight during the summer, but rotating to earlier MLT (clockwise) in the winter, and then back to later MLT in the spring. The band of occurrence was spread around a greater range of MLT during the winter than summer. The band of echoes is due to half-hop echoes from F-region irregularities in the auroral oval and polar cap.
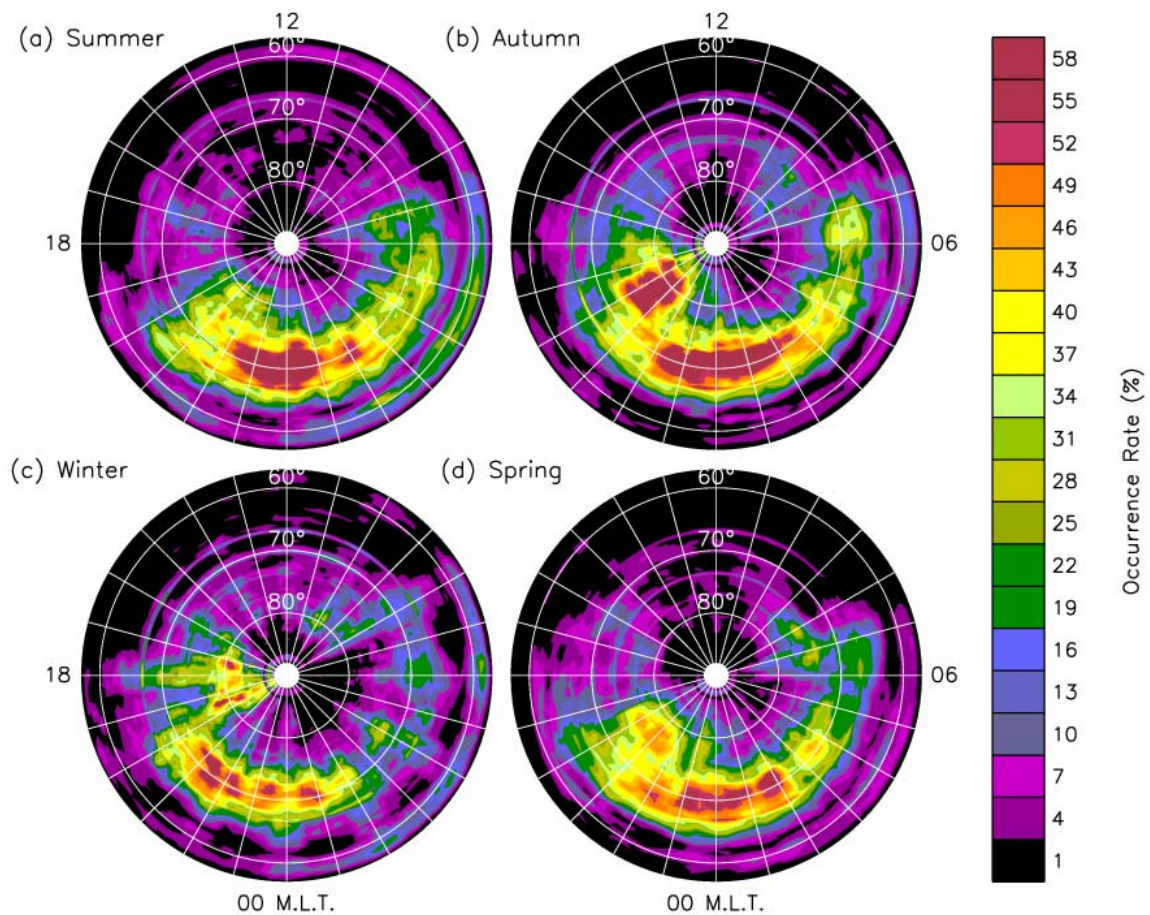
Figure 3.3: The occurrence rate of beam 4 ionospheric echoes for all K_p values for (a) summer, (b) autumn, (c) winter, and (d) spring of year 2000.

The importance of HF propagation conditions in affecting the observations can be highlighted by the presence of a substantial patch of echoes located near dusk, ~20 MLT in autumn and spring, and 18 MLT in winter. These echoes have a greater range than the main band of nightside echoes and extend deeper into the polar cap. They were detected via "one-and-a-half hop" propagation. The ionosphere is generally weaker during the night and therefore a lower frequency is required to obtain

backscatter. TIGER compensates for this by decreasing the operating frequency. Thereafter half-hop echoes were obtained.

Another seasonal dependence is apparent. There was a smaller band of maximum occurrence and a greater spread in the lower occurrence rates during winter than in summer. The equatorward boundary of high occurrence was at higher latitudes in the winter.

A comprehensive set of plots showing how the occurrence rates varied from season to season and month to month are given in Appendix A.

3.2 Average power

Figure 3.4 shows a map of occurrence rates and the average powers returned by the FITACF algorithm for ionospheric echoes with a signal-to-noise ratio >3 dB for the contrasting years 2000 and 2003. Average FITACF parameters are not shown in this and subsequent sections if fewer than 2 valid FITACF results were obtained per time bin. Even so, most of the averages have a small relative error because they are based upon numerous samples. Figure 3.4 shows the strong association between features with higher average power and higher occurrence rate. Much like the occurrence rates, the powers declined from year 2000 to 2001, and then increased slightly in 2002, followed by a more dramatic decrease in 2003. Moderate average powers also spread around to more MLTs at sunspot minimum. However, during all years the average powers were enhanced at the equatorward edge of the main band of occurrence (i.e., ~67°), and then decreased gradually toward the geomagnetic pole.
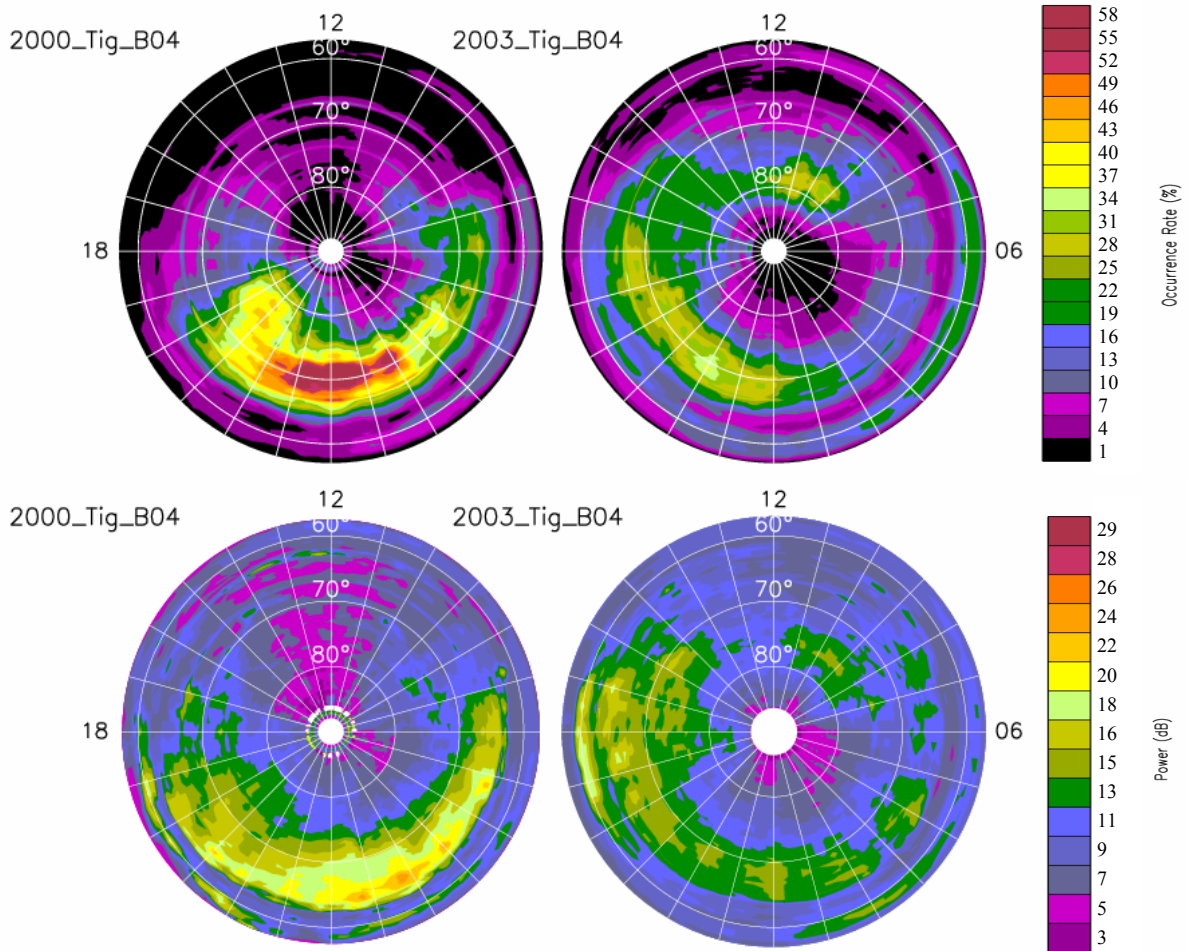
Figure 3.4: Occurrence rates and average powers for years 2000 and 2003.

When the powers were sorted according to season and K_p, variations similar to those for occurrence rates for each year were found. For example, Fig. 3.5 shows a map of the average powers for each season in 2001, and all levels of geomagnetic activity. Like the occurrence rates, all years revealed that autumn had the strongest powers spread over the greatest region, followed by spring, winter, and lastly summer. The average powers were especially weak in the post noon sector during summer, and the distributions of peak power tended to be shifted post midnight. During winter, there were low powers in the dayside again, and perhaps the peak power distribution was rotated pre-midnight. Summer recorded the lowest average peak powers for each year.
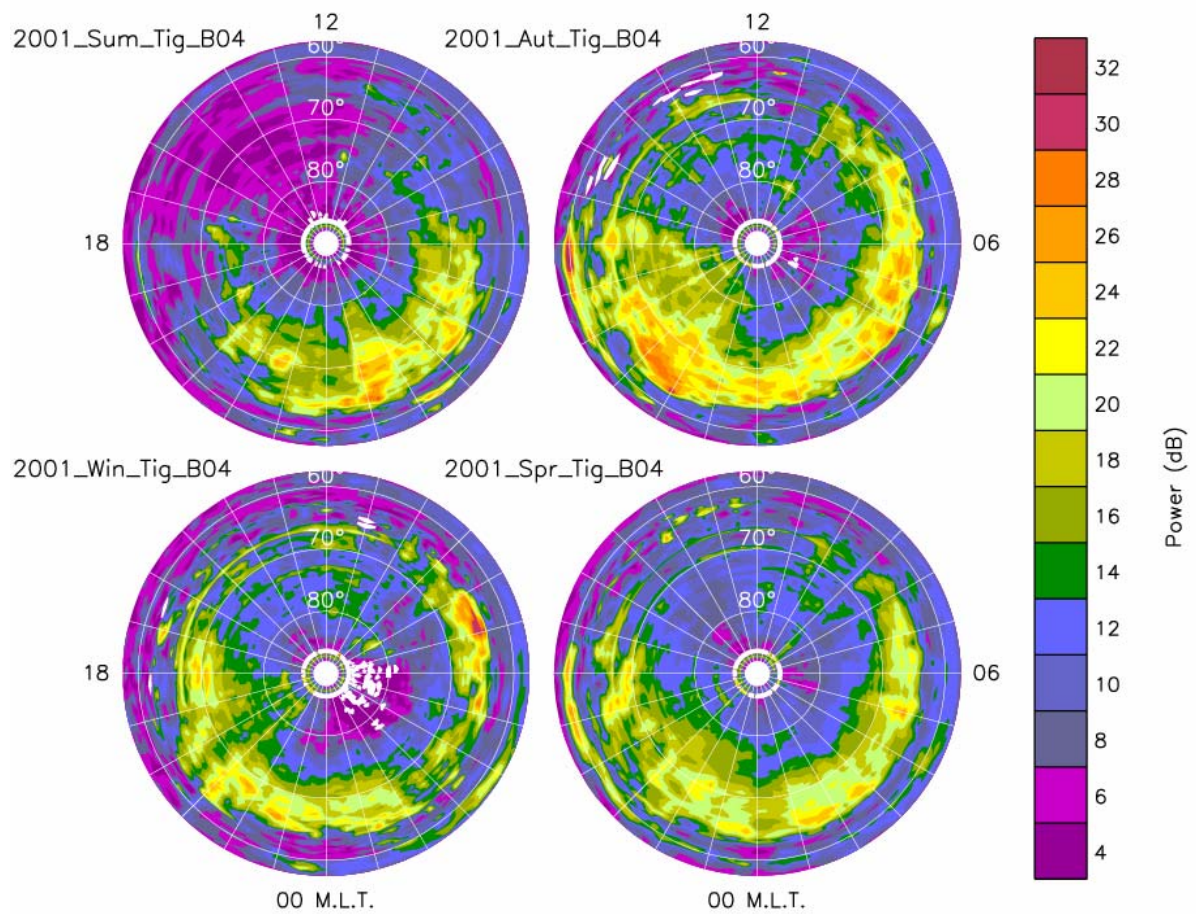
Figure 3.5: Average power of beam 4 ionospheric echoes for all K_p values detected during (a) summer, (b) autumn, (c) winter, and (d) spring of 2001.

These results are similar to some of those obtained in other studies such as those conducted by Ruohoniemi and Greenwald (1997), Milan *et al*. (1997), and Parkinson *et al*. (2003). The associations are reasonably clear for the yearly averages, but are not as apparent when looking at shorter time intervals because of statistical noise (see Appendices A and B for a comprehensive set of plots of monthly occurrence rate and average powers, respectively).

3.3 Line-of-sight Doppler velocities

Line-of-sight (LOS) Doppler velocities are a measure of the movement of ionospheric irregularities. Figure 3.6 shows the average LOS velocities for each year. One major feature of the high latitude ionosphere was represented in every time interval examined, namely the cross polar jet. Its existence was revealed by the large negative velocities observed pre-noon and large positive velocities observed pre-midnight.

When sorted according to season, solstice and equinox, or month, the maps of average LOS velocity show similar variations to those in Fig. 3.6. However, the region of large poleward velocities, centred pre-noon and pre-midnight, are clearly more widespread during year 2000 than 2002 and 2001, and they are more confined in 2003.
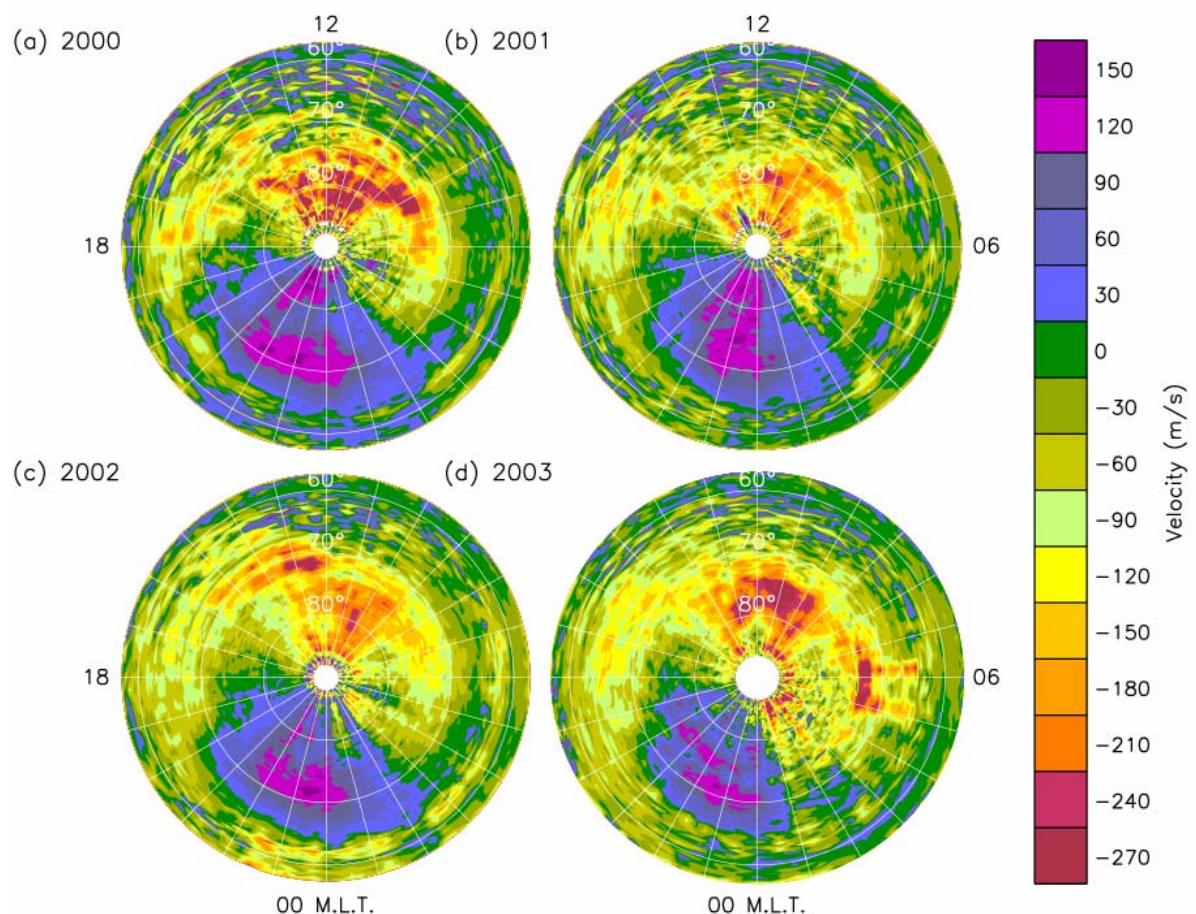
Figure 3.6: Average LOS Doppler velocity for beam 4 ionospheric echoes for all K_p values detected during (a) 2000, (b) 2001, (c) 2002, and (d) 2003. Negative and positive velocities are away and towards the radar, respectively.

3.4 Spectral widths

Figure 3.7 shows the average Doppler spectral widths for all seasons and levels of geomagnetic activity combined. In previous case studies, spectral widths have been used as a means to identify the ionospheric signature of magnetosphere regions or boundaries (e.g., Baker et al., 1995 and Villain et al., 2002).
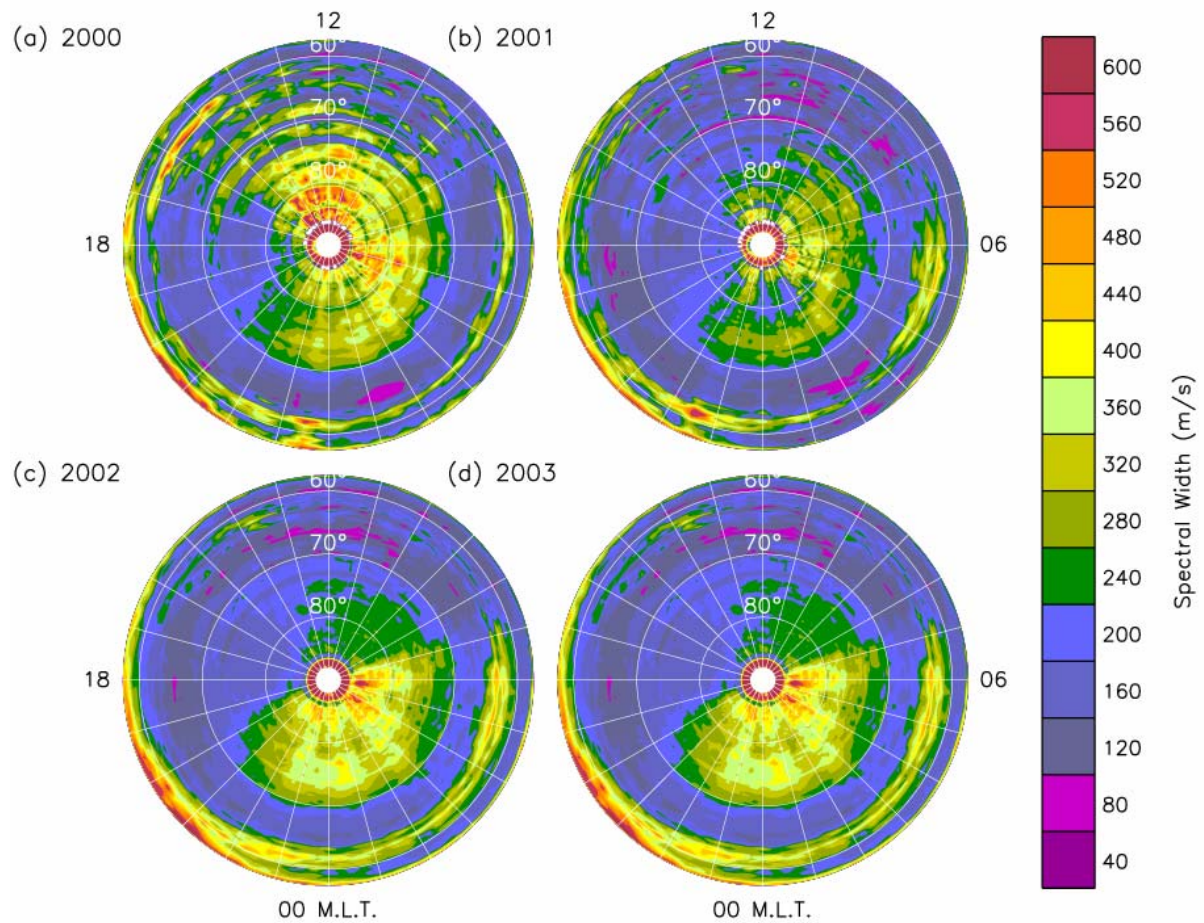
Figure 3.7: Average Doppler spectral widths for beam 4 ionospheric echoes for all K_p values detected during years (a) 2000, (b) 2001, (c) 2002, and (d) 2003.

The distribution of spectral widths seems independent of the other radar parameters. Larger average spectral widths were concentrated around the polar cap and auroral region over all years. In 2000 large spectral widths (>300 ms^{-1}) were found from 21 to 16 MLT within ~20° of the pole. There were some extremely high widths at very close ranges in the pre-midnight sector. These features reoccurred in 2001, albeit if the average spectral widths were much lower. In 2002 the distribution of large

spectral widths was limited to the nightside, covering only 11 hours. In 2003, the distribution spread back into the dayside, but the largest average widths were in the nightside polar cap. Year 2000 had the most extensive regions of large spectral width, and 2001 had the smallest spectral widths.

At the time of writing, the variability in spectral widths were not fully understood, although some might be attributed to variations in the version of FITACF used to process the data in near real time, as well as to genuine geophysical variability related to coupling between the ionosphere and magnetosphere.

3.5 Discussion of results

The decrease in the number of echoes was partly arrested during 2002 which had generally slighty higher scatter rates over a greater area. A secondary maximum in the sunspot number, noted in Fig1.1, might also be associated with this effect. It is thought that larger plasma densities in the F-region due to more photo-ionisation provides for greater refraction of HF radio waves and thereby leads to the detection of more decametre scale irregularities at sunspot maximum. However, for some unknown reason, the irregularity occurrence may also be greater at sunpot maximum.

The data also reflects upon a change in the common time radar control programs, with *"normal_scan"* and *"fast_scan"* being replaced with *"normal_sound"* and "*fast_sound*" in April 2002. The latter programs had greater frequency agility and allowed a greater number of echoes to be detected at all MLTs, especially on the dayside. Hence the effects of changing radar operations, HF propagation conditions, and irregularity occurrence are confounded.

In general, the patterns of occurrence appeared most like those for moderately disturbed conditions, K_p = 1~3 (i.e., this is the most frequently or "mode" pattern) (Fig. 3.3). Under more disturbed magnetic conditions, there can be enhanced absorption of radar signals due to ionization of the D-region, and there can be screening of propagation to the F-region by enhanced E-region ionization. The

occurrence rates became patchy but unusually high under heavily disturbed geomagnetic conditions. This is because the rates were calculated using a progressively smaller amount of data for increasingly larger storms. The auroral oval expanded as there was a lot of E and F region scatter at close ranges, and the remaining scatter from the polar cap was patchy, but locally intense.

In general, ionospheric echoes became slightly less intense though more spread in MLT during the winter when the magnetic pole was tilted away from the solar wind (Fig 3.3). An unexpected feature appeared during the winter months of 2003, with lower than usual occurrence rates (<20%) between 00 and 08 MLT (See Appendix A for monthly occurrence rates). A possible explanation is that the F-region plasma densities became too low to adequately support refraction in the winter at sunspot minimum. Reasonable ionospheric scatter may have been obtained pre-midnight because the ionisation levels were still adequate.

The relatively low occurrence rates on the dayside might be due to the predominance of photoionisation which can affect ionospheric backscatter in a number of ways. For example; increased densities in the D and E-regions lead to stronger absorption of radio waves. This decreases the signal-to-noise ratio of the backscattered signal. Gradients in F-region plasma density and thus ionospheric instabilities are reduced by relatively uniform ion production. The conductivity of the enhanced E-region tends to dampen F-region irregularities (Ruohoniemi and Greenwald, 1997). Numerous ionospheric echoes may be detected on the dayside, but they were classified as groundscatter, and therefore not included in this study.

A trough in echo occurrence tended to occur in the nightside ionosphere centred on about –62° magnetic (Fig 3.1, 3.2, 3.3). This trough arises because of the separation between the preferred range windows for half-hop E and F-region scatter. These preferred range windows arise because the prevailing HF propagation conditions support refraction of the radio waves to normal incidence on the magnetic field lines at predictaible locations. A gap in these predictable locations occurs in the presence of the valley or ledge separating the E and F region layers. The ionospheric irregularities can also be concentrated at preferred altitudes.

The dominant mechanism for ionospheric irregularity transport was seen to be the cross polar jet, which results from the dawn-dusk electric field created by the solar wind and the IMF interacting with the magnetosphere and ionosphere. The resulting $\mathbf{E} \times \mathbf{B}$ drift is across the pole from the dayside to the nightside. Under quiet solar and geomagnetic conditions, the drift is relatively small, even sunward. However, for more disturbed conditions the size and strength of the jet are amplified. Sorting the maps of average LOS velocity according to B_z or K_p confirmed this belief. A standard two-cell convection pattern is also apparent in the maps of average LOS velocity (Fig. 3.6). The flows were near zero in the dawn and dusk sectors, consistent with zonal return flows directed sunward at latitudes below the convection reversal boundary and antisunward above. These motions are consistent with clockwise and anticlockwise flowing cells in the dusk and dawn sectors, respectively.
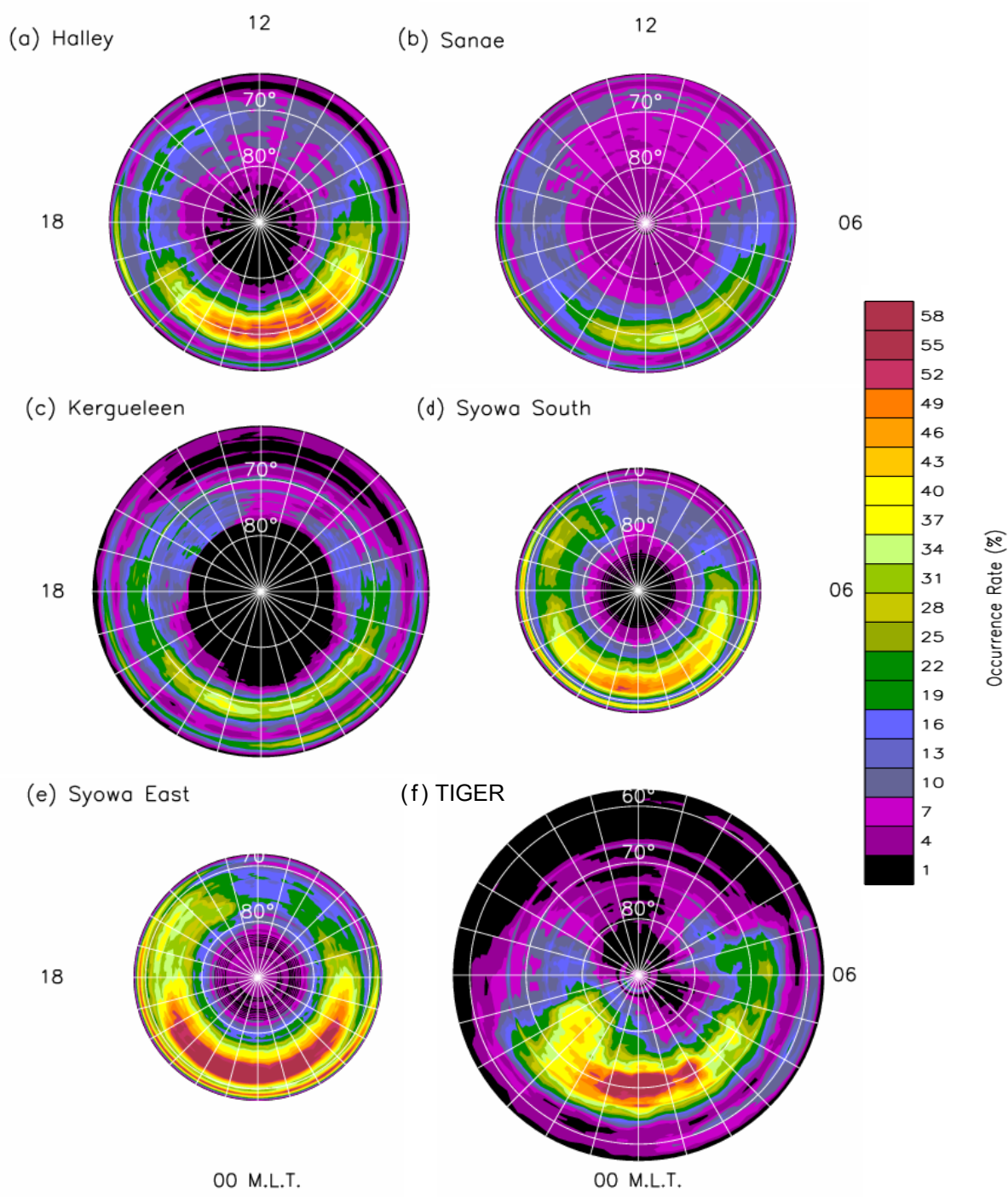
Chapter 4: **SOUTHERN HEMISPHERE RADARS**

TIGER is one of the six Southern Hemisphere SuperDARN radars that operated for at least half of the year 2000. The design of all of these radars was based upon the original radar located in Goose Bay, Labrador (Greenwald et al., 1985). A statistical analysis of observations made by different SuperDARN radars permits a more detailed investigation into various parameters affecting the occurrence of ionospheric scatter, such as radar longitude and latitude, and pointing direction. Also, any physical interpretations of the results must be consistent with the results obtained for all the radars.

Again, databases were compiled for the beams which pointed along the magnetic meridian following the procedures outlined in Chapter 2. Syowa East's field of view did not point toward the south geomagnetic pole, therefore the beam closest to the magnetic meridian was chosen. The same programs used to produce plots of TIGER data were manipulated to create equivalent plots for the other radars. Table 5.1 is a summary of the different stations used and key software parameters including conversions to magnetic coordinates.

Station	Abbreviation	Station Id.	CGM Long.	UT to MLT	Beam Number
Halley	hal	4	29.09	0.886806	8
Sanae	san	11	42.55	0.925694	12
Syowa South	sys	12	71.11	0.006944	13
Syowa East	sye	13	71.11	0.006944	0
TIGER	tig	14	226.9	0.43403	4
Kerguelen	ker	15	122.60	0.131806	11

Table 4.1: Radar station, abbreviation used to separate data files, identity number, geomagnetic longitudes, conversion from Universal Time to Magnetic Local Time, and the magnetic meridian beam number of each station.

The Halley and TIGER radars produced file sizes (and thus numbers of echoes) that were four times larger than the other radars. This is because both these radars used the same discretionary mode RCP which interleaved soundings on the magnetic meridian beams between other beams in the full scan, e.g. for TIGER: beam 15, 4, 14, 4, 13, 4,…. Hence far more echoes were recorded on their meridional beams. The Syowa

Figure 4.1: Occurrence rates of ionospheric echoes along the nearest magnetic meridian beam and for all K_p values for the Southern Hemisphere SuperDARN radars during 2000 (a) Halley, (b) Sanae, (c) Kerguelen, (d) Syowa South, (e) Syowa East and (f) TIGER.

East radar had the next largest files, followed by Syowa South, and Kerguelen. The Sanae radar provided the smallest file sizes. The Kerguelen radar started recording data in the middle of 2000, so the complete seasonal variation was not obtained for this radar. Despite the file size differences, similar changes in occurrence and Doppler characteristics were found for all radars.

Figure 4.1 shows the occurrence rates from the six southern SuperDARN radars listed in Table 4.1. The results for TIGER are reproduced again to permit direct comparison with the results obtained for the other radars. The figure reveals that nightside scatter from the auroral oval and the polar cap dominated for all radars. The maximum occurrence rates were roughly centred near magnetic midnight and ~20° or less from the geomagnetic South Pole. For all the radars except the zonal looking Syowa East radar, the main band of maximum occurrence was shifted slightly anticlockwise into the post-midnight sector. This is especially apparent for the Halley and Sanae radars. A clear minimum can be seen near midday for all radars at all ranges.

The maximum occurrence rates were found closer to the pole if the radar was located closer to the pole, probably because of the preferred range window effect. And higher averages were obtained across a greater range of MLT for the radars located closer to the pole. More dayside echoes were also recorded for those radars closer to the pole. This might be because the zone of intense irregularities in the auroral and polar cap ionosphere was accessible via mostly half-hop propagation for these radars.

Conversely, the maximum occurrence rates were confined to smaller regions for the more equatorward radars. For example, TIGER's maximum occurrence rates spanned ~5 h while Syowa East's spanned ~9 h. The scatter for TIGER was exceptional in that it had a small intrusion of half-hop echoes towards the pole at ~21 MLT. All of this suggests that radars located even further equatorward than TIGER will only access intense irregularities near magnetic midnight and especially during major storms.
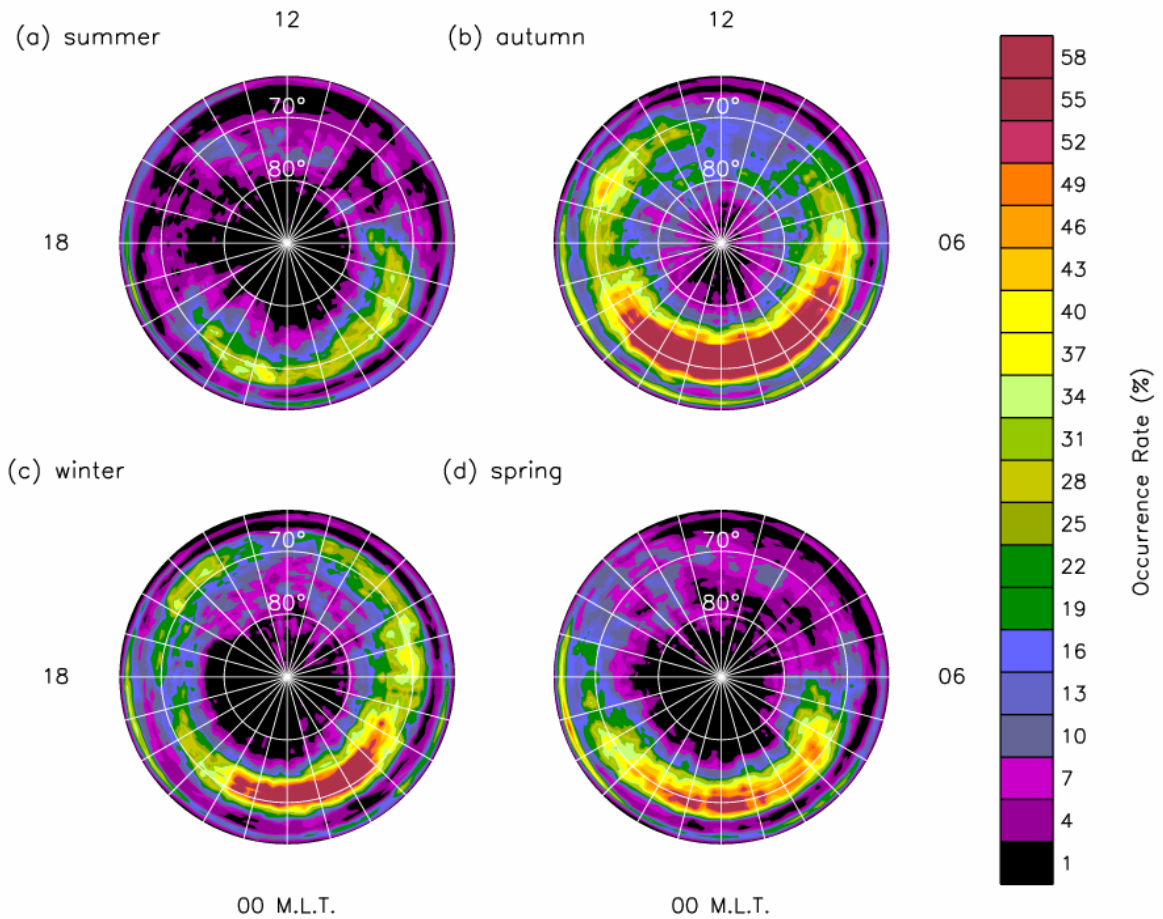
Figure 4.2: Representative occurrence rates of ionospheric echoes along the nearest magnetic meridian beam and for all K_p values during (a) Summer, (b) Autumn, (c) Winter, and (d) Spring 2000. Results for the Halley radar are shown.

Seasonal dependencies are unveiled in Figs. 4.2 and 4.3. The nightside bands of maximum occurrence were strongest during autumn, then winter, spring, and lastly summer. The bands of high occurrence were strongest and most extensive in MLT during autumn and winter. The exception was Kerguelen which had the most extensive occurrence during summer, possibly due to the radar being operational after June 2000. TIGER also had maximum occurrence during autumn, and then summer had very high occurrence, though localised near midnight. All of the nightside bands of maximum occurrence tended to be shifted post midnight.
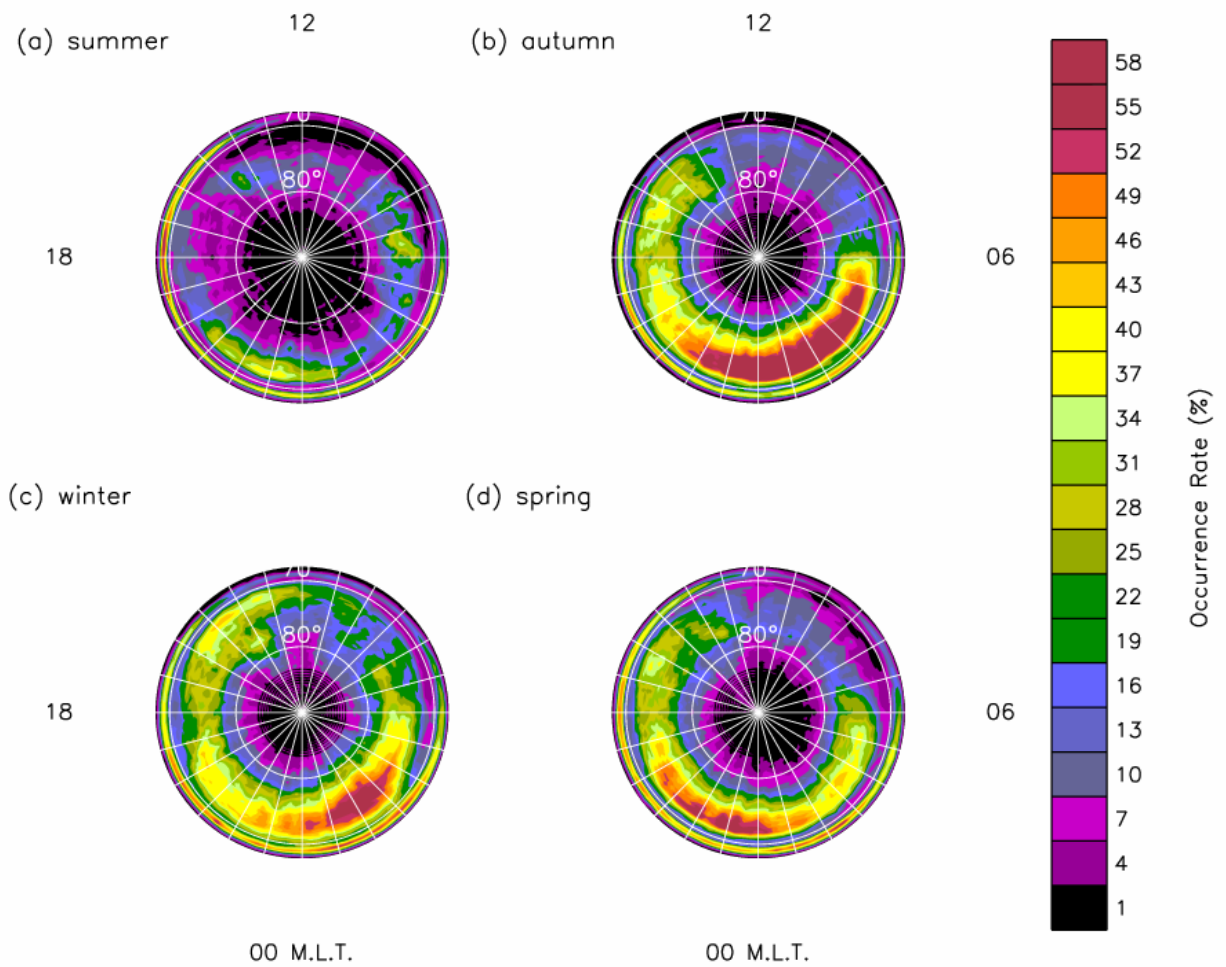
Figure 4.3: Representative occurrence rates of ionospheric echoes along the nearest magnetic meridian beam and for all K_p values during (a) Summer, (b) Autumn, (c) Winter, and (d) Spring 2000. Results for the Syowa South radar are shown.

Several factors were confounded to produce the seasonal variations shown here. On the one hand geomagnetic storms are known to occur more frequently near the equinoxes. The solar zenith angle also modulated the occurrence patterns, confining peak occurrence rates closer to midnight during the summer. The thin bands of occurrence situated at close ranges from late afternoon to dawn were probably from E-region irregularities and meteors, and their variability should be considered separately.
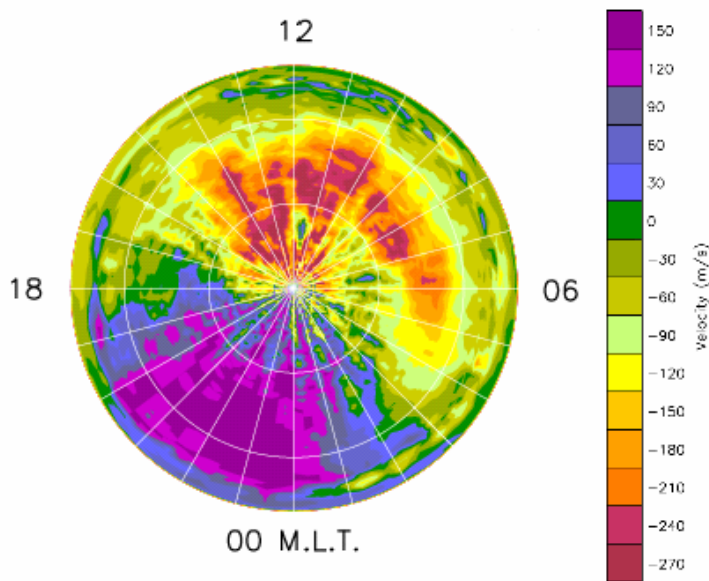
Figure 4.4: Representative average LOS Doppler velocities for a magnetic meridian pointing beam and all K_p values detected during 2000. Results for the Halley radar are shown.

Figure 4.4 shows a representative plot of average LOS Doppler velocities which revealed the familiar cross polar jet. Large velocities were observed heading away from the radar pre-noon, and towards the radar pre-midnight. When looking at data from each radar, and sorting them according it to season and month, the patterns of average velocity were consistent with the prevailing movement of irregularities in the expected **E**×**B** direction.
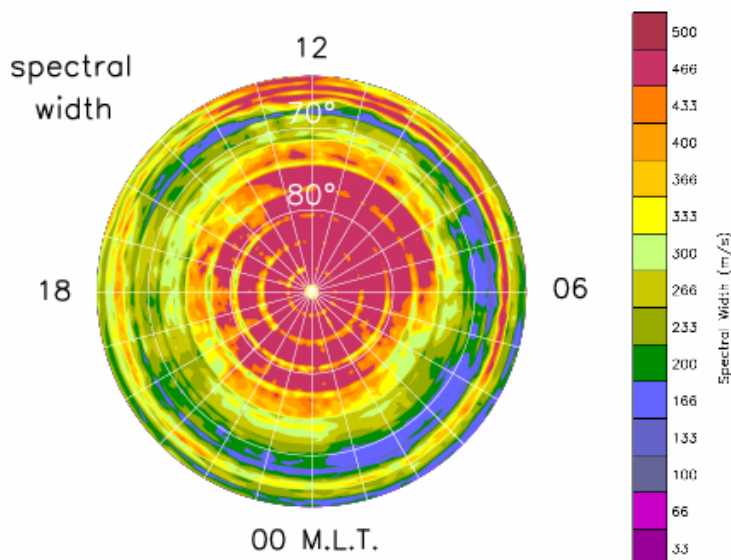
Figure 4.5 Representative average LOS Doppler spectral widths for a magnetic meridian pointing beam and all K_p values detected during 2000. Results for the Halley radar are shown.

Figure 4.5 shows a representative plot of average spectral widths for the year 2000. A region of high spectral widths confined to high polar cap latitudes is noted. However, it is extended to lower latitudes in the pre-noon sector. A trough in the average spectral widths (~166 m s^{-1}) encircled the polar cap region of large spectral widths. This trough was centred near 64° near noon, and near 68° near midnight. The spectral widths rose sharply at the poleward edge of this feature.

The region of high spectral widths over the polar cap form concentric rings centred on the pole. These rings must arise because of sensitivity of the FITACF algorithm to bad ranges and bad lags which are a consequence of the pulse-set technique. Because this technique is not very robust, there is a possibility that different radars will measure different absolute values of spectral width due to subtle differences in the engineering of the radars. Again, the spectral width patterns are very complex and the boundary layer physics responsible for them are not fully understood at the time of writing.

Detailed plots of occurrence and Doppler characteristics of monthly, seasonal and yearly plots from Halley, Sanae, Syowa South, Syowa East, and Kerguelen can be viewed in Appendices 5, 6, 7, 8 and 9 respectively

4.1 Discussion of results

Data recorded with all the Southern Hemisphere SuperDARN radars displayed similar statistical patterns to TIGER (cf. Chapter 3). Although some of the differences might be explained by the different longitude, latitude, and pointing directions of the radars (e.g., the more zonal pointing Syowa East radar), the similarities in the statistical patterns must reflect upon the underling spatial and temporal variability in the occurrence of ionospheric irregularities. For example, nearly all of the radars observed a band of maximum echo occurrence in the nightside ionosphere at auroral and polar cap latitudes. This must be an intense irregularity zone which the different radars image in a slightly different way because of the different preferred range windows for irregularity detection.

The mid-latitude TIGER and Kerguelen radars recorded relatively few echoes during the day. This is in contrast with the higher latitude Syowa South and Syowa East radars which demonstrated many irregularities are present in the dayside high-latitude ionosphere. The more equatorward radars struggle to observe irregularities in the dayside ionosphere, and must access the intense irregularity zone via one-and-half hop propagation. For example, intense irregularities generated in the cusp region of the auroral oval are located closer to the pole than intense irregularities generated in the nightside auroral oval.

During the summer months at high latitudes the Sun remains in the sky, albeit at low elevation angles, almost all the time. This results in a smoother ionosphere with fewer density gradients conducive to irregularity formation, and a stronger D-region ionosphere which absorbs more of the transmitted signal. This is part of the explanation as to why the minimum occurrence rates for all radars are found on the dayside during the summer months.

Figure 4.3 confirms that the cross polar jet was the dominant feature responsible for the transportation of decametre scale irregularities across the polar cap ionosphere. A standard two-cell convection pattern was also implied by the average LOS velocities. There were high velocities either side of the pole with the appropriate sign at noon or midnight, and the velocities were near zero in the dawn and dusk sectors. The latter motions are consistent with underling clockwise and anticlockwise rotation in the dusk and dawn sectors respectively.

Chapter 5: **SUMMARY AND FUTURE WORK**

5.1 Summary

It is known that the Sun, although extremely far away, exerts a tremendous influence on processes occurring at Earth. It was discussed how the Sun releases the solar wind and the imbedded IMF, thus mediating a direct effect on the Earth, its magnetic field, and in turn the upper atmosphere. It was also discussed how SuperDARN radars can gather information about the ionosphere from the presence of decametre-scale irregularities, which are influenced by solar particles, electromagnetic radiation, and the IMF. Then it was revealed how the information recorded by SuperDARN radars can be analysed in a useful statistical way to help provide evidence constraining the mechanisms responsible for generating disturbances in the auroral and polar cap ionospheres.

One of the most important results of this study was the extent to which the Sun controls the occurrence of HF radar echoes from decametre scale irregularities in the high-latitude ionosphere. From the results it was discovered that the occurrence of ionospheric echoes was strongly influenced by the solar cycle as measured by the sunspot number. For example, the occurrence rates and powers were largest during the sunspot maximum year 2000, and generally declined through to the sunspot minimum year 2003. Although this effect was seen most clearly from a comparison of occurrence rates and powers from one year to the next, some of the variations from one season to the next were also associated with fluctuations in sunspot number.

The dependency of SuperDARN echo occurrence on solar activity is thought to be related to changing F-region plasma densities and thus HF propagation conditions (due to changes in solar UV and X-ray fluxes). However, we speculate that some of this dependency may be due to changes in the intensity and frequency of decametre scale irregularities with solar activity. This is because the radars can change their operating frequency to compensate for changing propagation conditions to some extent, and yet there is still a dependency of echoes on solar activity.

Other influences that affected the occurrence of ionospheric echoes included changes in the operating mode and frequency of the radar, and seasonal factors. The latter included the variability in irregularity occurrence and HF propagation conditions due to seasonal and diurnal variability in the solar zenith angle, and the effects of changing dipole tilt angle, with peak occurrence rates in the autumn and spring equinoxes, perhaps related to the familiar enhancement of geomagnetic activity near these times. It is thought that coupling between magnetic clouds in the solar wind and the magnetosphere is more affective near to the equinoxes because antiparallel merging is more readily satisfied at these times (Russel, 1973).

It is only possible to reach tentative conclusions about the ultimate causes of decametre-scale irregularities using the statistics presented in this thesis. However, it is interesting that all of the radars tended to observe a shift of the peak nightside occurrence rates toward post-midnight (Figs. 4.1 & 4.2). A similar shift was found for the backscatter powers. However, the peak nightside occurrence rates tended to decline and shift toward dusk with declining solar activity (Figs. 3.1 & 3.4). Perhaps intense irregularities could not be observed in the post-midnight sector during the winter at solar minimum because the F-region ionosphere was just too weak to support propagation at the lowest radar operating frequencies.

Because the above effect was found for most radars located at different locations, it suggests that there is a genuine bias towards more frequent and intense ionospheric irregularities in the post-midnight sector. This lends further support to the notion that the ionospheric slip velocity — the motion of F-region plasma relative to the neutral wind — plays a significant role in regulating the gradient drift instability (Tsunoda, 1988; Parkinson et al., 2003). Note that ionospheric absorption is not necessarily weaker post-midnight because hard electron precipitation extends to the equatorward edge of the auroral oval.

A single SuperDARN radar like TIGER can provide important insights into many of the disturbances affecting the high latitude ionosphere. However, cross referencing the data recorded by many different radars can increase confidence in any theories invoked to explain the observed variability. There is a danger that the variability observed by a single radar is merely in agreement with an explanation by chance

alone. Many of the preceding explanations were consistent with the variability observed by most of the radars.

In summary, this thesis has shown that many factors affect the likelihood of observing HF backscatter from decametre scale ionospheric irregularities. It can be theorized that the consequential effects of solar activity (sunspot cycle) on geomagnetic disturbance level, the solar-zenith angle, HF propagation conditions, and the state of the background neutral atmosphere strongly influence the production, dissipation, and detection of ionospheric irregularities.

5.2 Future Work

SuperDARN radars and especially the TIGER radar supply a wide variety of knowledge about the high-latitude ionosphere. The following points list items worthy of future investigation:

(1) Clock dial plots of average operating frequency and the variance in those operating frequencies will provided further insights into the effects of changing radar operating mode and HF propagation conditions.

(2) The occurrence rates and Doppler characteristics need to be directly sorted according to sunspot number and 10.7 cm solar flux, using even more data than analysed here.

(3) The study could be extended to the analysis of the data recorded by all of the Northern Hemisphere radars in the same way. For example, the analysis of the data recorded by the magnetically conjugate King Salmon and TIGER radars would be especially helpful in understanding seasonal changes.

(4) The results for zonal pointing beams need to be sorted in the same way to provide information on directional effects — the growth of ionospheric irregularities and their Doppler characteristics are not necessarily isotropic.

(5) The results for the NZ Unwin radar will need compiling, and will complement the results of the existing TIGER radar, especially in regards to directional effects.

(6) Statistics on the occurrence of scintillations measured using the GPS receiver at Macquarie Island can be compiled in a similar way, and will provide important

information on the variability of kilometre scale irregularities. This will help provide insights into variability of the decametre scale irregularities which grow upon these larger scale gradients. This study would help to separate out the effects of changing HF propagation and changing irregularity intensity.

(7) About 99% of the upper atmosphere is a neutral gas, and as such the ionosphere can be considered a weakly ionised plasma. Ionospheric irregularities can be affected by the neutral winds. Concurrent measurements of the neutral winds will provide further insights into irregularity formation and backscatter occurrence.

(8) Mechanisms responsible for the spectral widths are in need of testing. The spectral widths raise many questions about the geophysical variability in the ionosphere and magnetosphere, suggesting the existence of a highly dynamical system in need of deeper understanding. With the aid of ground based and satellite electric field probes and magnetometers, electric field fluctuations and ULF wave activity could be analysed and related back to variability in the spectral widths.

(9) Of course, when different radar observations of the same event are examined, the occurrence of scatter on short time scales can have similar or completely different characteristics to those represented in the statistical plots of this thesis. More case studies need to be examined to help interpret the statistics.

BIBLIOGRAPHY

ACE Science Center 2003, The Advanced Composition Explorer (ACE) Science Center [web page] http://www.srl.caltech.edu/ACE/ASC/

Alvestad, Jan. 2004, Solar Terrestrial Activity Report, Solar cycles 21, 22 and 23 [web page] http://www.dxlc.com/solar/solcycle.html

Balthazar, R. SPARG, Space and Atmosphere Research Group, University of Sheffield [web page] http://www.shef.ac.uk/~sparc/

Barker, K.B., J.R. Dudeney, R.A. Greenwald, M. Pinnock, P.T. Newell, A.S. Rodger, N. Mattin and C. Meng 1995. "*HF radar signatures of the cusp and low-latitude boundary layer.*" J. Geophys. Res. vol. 100, pp. 7671-7695.

Barnes, R. SuperDARN, [web page] http://superdarn.jhuapl.edu/index.html

Chen, F.F. 1984. "*Introduction to plasma physics and controlled fusion.*" New York: Plenum Press.

Dyson, P.L. and J.C. Devlin 2000. "*The Tasman International Geospace Environment Radar*". The Physicist (The Australian Institute of Physics), vol. 37, pp. 48-53.

Dyson, P.L., J.C. Devlin, M.L. Parkinson, J.S. Washington 2003. "The Tasman International Geospace Radar (TIGER) – Current development and future plans." IEEE Proceedings of the International Conference on Radar, pp. 282-287.

Greenwald, R. A., K.B. Baker, R.A. Hutchins and C. Hanuise 1985. "An HF phased-array for studying small scale structure in the high-latitude ionosphere." Radio Sci., Vol. 20, pp. 63-79.

Greenwald, R. A. 1995. "*DARN/SuperDARN: A global view of the dynamics of high latitude convection.*" Space Sci. Rev., vol.71, pp. 761-796.

Hargreaves, J.K. 1992. "*The solar-terrestrial environment.*" Cambridge: Cambridge University Press

Høymork, S. 2000. Research in Space Physics at IRF [web page] http://www.irf.se/rpg/science/picts/Magnetosphere.gif

IGRF/DGRF Model Parameters and Corrected Geomagnetic Coordinates [web page] http://nssdc.gsfc.nasa.gov/space/cgm/cgm.html

Kelly, M.C., J.F. Vickrey, C.W. Carlson and R. Tobert 1982. "*On the origin and spatial extent of high-latitude F region irregularities.*" J. Goephys. Res., vol. 87, No. A6, pp. 4469-4475.

Milan, S.E., T.K. Yeoman, M. Lester, E.C. Thomas and T.B. Jones 1997. "*Initial backscatter occurrence statistics from CUTLASS HF radars.*" Ann. Geophys.., vol. 14, pp. 703-718.

Ruohoniemi, J.M., R.A. Greenwald 1997. "*Rates of scattering occurrence in routine HF radar observations during solar cycle maximum*" Radio Sci., vol.32, num.3, pp. 1051-1070.

Russel, C.T. and R. L. Mc Pherron 1973. "*Semiannual variation of geomagnetic activity*" J. Geophys. Res., Vol. 78, No. 1, pp. 92.

Tsunoda, R.T. 1988. "High-*latitude F region irregularities: A review and synthesis.*" Rev. Geophys., vol. 26, pp. 719-760.

Parkinson, M.L., J.C. Devlin, H. Ye, C.L. Waters, P.L. Dyson, A.M. Breed and R.J. Morris, 2003. "*On the occurrence and motion of decametre-scale irregularities in the sub-auroral, auroral, and polar cap ionosphere.*" Ann. Geophys., vol. 21, pp. 1847-1868.

Papitashvili, V., N. Papitashvili and R. McGuire 2001. IGRF/DGRF Model Parameters and Corrected Geomagnetic Coordinates [web page] http://nssdc.gsfc.nasa.gov/space/cgm/cgm.html

Villain, J.P., R. Andre, M. Pinnock, R.A. Greenwald, and C. Hanuise 2002. "*A statistical study of the Doppler spectral width of high-latitude ionospheric echoes recorded with SuperDARN coherent HF radars.*" Ann. Geophys., vol. 20, pp. 1769-1781.

Zielik, M., S.A. Gregory and E.V.P. Smith 1995. "*Introductory Astronomy and Astrophysics*", #rd edition. Saunders College Publishing, USA.

Links to TIGER websites where summary data can be easily accessed
http://plasma.newcastle.edu.au/spwg/research/tiger/tiger.htm

http://www.tiger.latrobe.edu.au/